Pergamon

PII: S0301-9322(97)00011-6

*Int. J. Multiphase Flow* Vol. 23, No. 5, pp. 899–925, 1997
Published by Elsevier Science Ltd
Printed in Great Britain
0301-9322/97 $17.00 + 0.00

# BEHAVIOR OF A POLYDISPERSE CLUSTER OF INTERACTING DROPS EVAPORATING IN AN INVISCID VORTEX

K. HARSTAD and J. BELLAN
Jet Propulsion Laboratory, California Institute of Technology, Pasadena, CA 91109, U.S.A.

*(Received 31 January 1996; in revised form 5 March 1997)*

**Abstract**—The dynamics and evaporation of polydisperse collections of liquid drops in an axisymmetric, infinite, cylindrical vortex are described using a statistical model. This model describes both the dense regime where inter-particle effects are important and the dilute regime. The initial size distribution is partitioned into size classes and each initial size-class is followed dynamically and thermodynamically using a class-defined, drop-frame coordinate system. Each initial-size-class develops a continuum of sizes as drops centrifuge towards hotter surroundings and evaporate. A separate coordinate system tracks the gas phase. Because larger drops experience larger centrifugal force, they approach the hotter gas faster. However, for appropriate liquid heating times, the large drops might evaporate at a faster rate, and so the size-differentiated centrifugation previously observed and calculated for cold flow situations does not occur. Instead, a radially peaked drop size distribution is developed in the gas vortex. The centrifugal motion forms a drop-free inner vortex core bound by a cylindrical shell containing all the drops. This shell of gas and drops is called the drop cluster. Numerical calculations show that more parameters control dense clusters than dilute clusters; examples of these parametric relations include: (i) the air/liquid mass ratio controls the inner cluster region and the gas vortex, whereas drop size distribution controls the outer region; and (ii) polydispersity increases the maximum mass fraction of the evaporated compound and enhances penetration of the evaporated compound into the surroundings. Except for dilute clusters, the assumption of uniform drop number distribution in the cluster is found to be inappropriate. Instead, the drop size distribution always becomes non-uniform even if the initial size distribution is monodisperse and the initial drop number distribution is uniform. This development of non-uniformity is caused by drops at the cluster peripheries preventing heat conduction/convection to drops in the central cluster. Published by Elsevier Science Ltd.

*Key Words:* drop clusters, evaporation, polydisperse, multiphase

## 1. INTRODUCTION

Particle-laden flows occur in many important situations: industrially relevant examples include the fuel sprays in Diesel engines, turbines, and furnaces while naturally occurring examples include tornadoes, dust storms and dust devils. The understanding of the particle-flow and the particle–particle interactions in such flows is directly related to control and/or prediction of quantities of interest. For example, current unsolved industrial problems are: optimization of gas turbine engines for efficiency and low nitric oxide emissions; optimization of Diesel engines for efficiency and low soot emissions; furnaces burning fuels having a range of volatilities and viscosities while controlling emissions.

Particle–particle interactions are unimportant if the particles are sufficiently distant from each other. 'Sufficient distance' is quantified by the ratio of the average half distance between adjacent particle centers, $R_i$, to the average particle radius, $R$. In previous studies (Bellan and Cuffel 1983), the ratio $R_i/R$ was called the 'nondimensional radius of the sphere of influence'. For large $R_i/R$, particles do not interact (dilute limit), but if $R_i/R \leqslant O(10)$ particle interactions become important (dense limit). The $R_i/R$ concept will be extended here to describe polydisperse collections of drops.

The interaction between particles and flow depends upon both mass loading and $R_i/R$. When the mass loading is low and $R_i/R$ is large, the flow affects the particles but not vice versa so that the dynamic influence of particles may be neglected when studying the flow, and particle interactions are not important. This limit has been studied by Crowe *et al.* (1988, 1993), Chung

and Troutt (1988) Lazaro and Lasheras (1989, 1992a, 1992b), Squires and Eaton (1991), Longmire and Eaton (1992), Tambour (1985), Greenberg *et al.* (1986) and Tambour *et al.* (1994). Some of these studies showed that large scale structures strongly affect particle dispersion and, for Stokes number $\approx 1$, particles accumulate at the structure edge (the 'focussing effect'). Yang and Sichel, 1989 modeled the interaction of a nonevaporating (nearly saturated), cylindrical droplet cloud with a swirling flow of an infinitely large region. The study was performed in the limit of very small drop volumetric fraction, constant drop temperature, no drop interactions, velocity of the gas within the cloud being much smaller than that of the drops, and initially monosize distribution. Seth *et al.* (1980) and Raju and Sirignano (1987) have also studied sprays in the absence of drop interactions.

This study presents results on *polydispersity, drop dispersion and evaporation combined with drop interaction*, issues of practical relevance to spray-combustion, medical sprays, spray dispensers and spray coating. Drop interaction is modeled from first principles and classes of drops defined by constant initial-size are followed in time and space to become polydisperse classes.

This configuration of a drop cluster in an inviscid vortex studied here is relevant to the spray edge where heat/mass transfer are important. Clusters of drops are entities observed in sprays produced by a variety of atomizers. Large, liquid clusters breaking into ligaments and droplets during atomization were observed by Engelbert *et al.* (1995) during the coaxial atomization of water in air. The velocity and diameter of these clusters were measured to be respectively 1500 cm/s and 0.4 cm, but their internal structure has not been determined. Akamatsu *et al.* (1996) have also observed droplet clusters in uniformly 'premixed' droplet streams, where premixed defined the condition of minimal slip velocity between drops and gas. The conclusion was that the existence of droplet clusters promotes the collective (group) burning of particles due to "their eddy motion and preferential flame propagation, hence generating temporal and spatial variation in the scale of droplet clusters". From the observed p.d.f. of the characteristic length scale of individual droplet clusters at a radial location of 1.5 cm and at several axial locations, an average characteristic length scale of droplet clusters versus the axial distance was calculated. This scale was shown to evolve from about 4.5 cm at a distance of 4.5 cm to about 0.3 cm at a distance of 13 cm. Despite these detailed observations, the internal structure of the clusters was not measured. Drop clusters in both burning and non-burning sprays were observed in a variety of situations (Allen and Hanson 1986a, 1986b; Rudoff *et al.* 1989; Mizutani *et al.* 1993; Nakabe *et al.* 1994) including air-assist sprays (McDonell *et al.* 1992, 1993). In burning sprays, flames were observed at the cluster periphery, suggesting the importance of drop interaction. Drops in vortices were also observed in burning sprays created by airblast atomizers (Hardalupas *et al.* 1994) and were determined to play a major role in the stabilization of the flame. Although individual groups of a small number of drops in streams or arrays have been experimentally studied, the structure of isolated clusters containing a large number of drops has never been experimentally characterized.

In this paper we adopt a dual point of view whereby: (1) the cluster of drops embedded in a vortex represents a physically limited region of a spray according to the above-cited observations; and (2) the structure of this limited region, which has not yet been determined experimentally, is modeled consistently with the physics of collections of drops in vortical flows. Such physical situations occur in sprays (Aftel *et al.* 1996; Presser *et al.* 1992, 1993, 1994; Presser and Semerjian 1988; Gupta *et al.* 1996; McDonell *et al.* 1992), although the spray conical geometric configuration does not have an exact correspondence to the axisymmetric configuration studied here. To ascertain that our model is physically correct, we seek experimental observations of our predicted quantities and compare their observed variation with our predictions. We consider that if we find similar variations in the experiments comparable to predictions, our model is qualitatively validated. Our focus is on the dynamics and thermodynamics of the gas and drops.

This paper is organized as follows: section 2 develops the system of equations, section 3 describes the method of solution, section 4 discusses initial conditions, section 5 presents numerical calculations and their interpretation, and section 6 gives a summary and conclusions.

## 2. PHYSICAL ASSUMPTIONS AND MODEL

A binary distribution of initial drop sizes in an isolated 2D axisymmetric infinite cylindrical vortex is shown as an example of the considered configuration in figure 1. For simplicity, all drops have identical initial temperature and the initial cluster gas temperature is uniform. The drops are much colder than the surrounding gas and have sizes and velocities depending on the radial position from the vortex center $r$ and on the time $t$. The initial size distribution is partitioned into distinct size classes identified by the subscript $j$ and each initial-size class is then followed in its own coordinate system. Since the drops evaporate while dispersed by the vortex, the drops in an initial-size class evolve into a continuum of sizes but remain in their respective initial-size class.

In the cold flow studies of Crowe *et al.* (1988, 1993), and Lazaro and Lasheras (1989, 1992a, 1992b) the drops did not evaporate and so dispersed differentially by size. In contrast, here drops do not necessarily disperse differentially by size because of a competing mechanism where larger drops, centrifuged further out, encounter hotter gas and might evaporate at a faster rate than smaller drops closer to the core. The competition between centrifugation and evaporation rate determines the particle size distribution for each class.

The cluster volume is bounded by surfaces which are the statistical envelopes of the outermost ($R_c$) and innermost ($R_{in}$) drops. This physical picture is suggested by the laser sheet beam measurements of Presser *et al.* (1993) for swirling pressure-jet sprays and of Presser *et al.* (1988) for both swirling pressure-jet nozzle and air-assist nozzle sprays which show an annular configuration of the horizontal cross section of the spray. Here the gas Reynolds number is defined as $\mathrm{Re} = u_G R_c / \nu_G$ where $u_G$ is gas velocity, $R_c$ is cluster radius, and $\nu_G$ is gas kinematic viscosity; typically $\mathrm{Re} \sim O(10^4)$ so that the vortex is inviscid. The drop Reynolds number is defined as $\mathrm{Re}_{dj} = u_{sj} R_j / \nu_G$, where $\mathbf{u}_{sj} = \mathbf{u}_{dj} - \mathbf{u}_G$ is the local slip velocity between phases, $\mathbf{u}_{dj}$ is the drop velocity and $R_j$ is the drop radius. Initially, $\mathrm{Re}_{dj} \sim O(1)$–$O(10)$ so that a drag force causes interaction between drops and gas. This force results from shape-drag, friction and drop evaporation and for the case of monodisperse drop clusters was found by Bellan and Harstad (1990) to be proportional to the drop number density. Bellan and Harstad's monodisperse deterministic model had drops uniformly dispersed in the cluster, dependent variables uniform through the cluster and used a

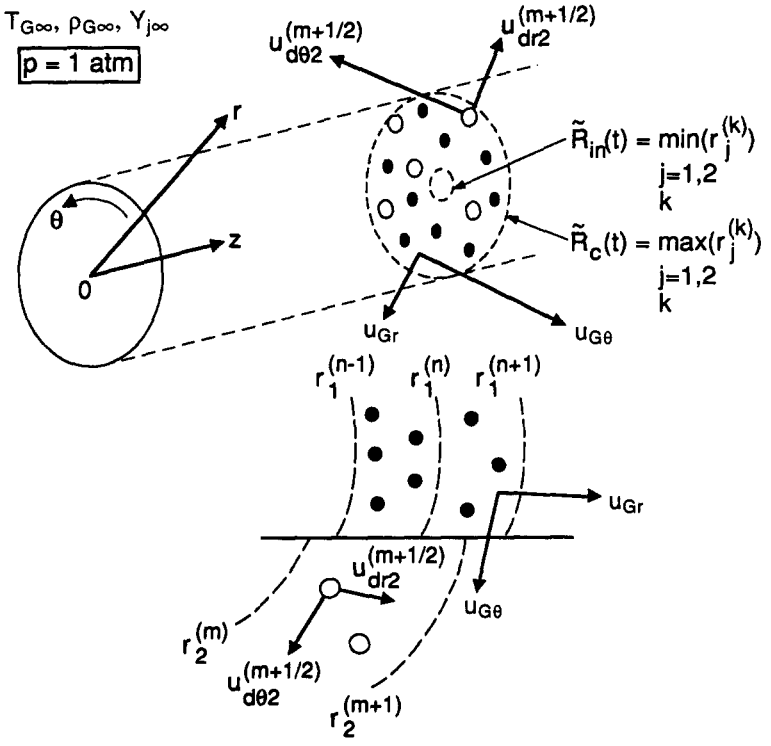


Figure 1. Sketch of a binary size configuration and of the coordinate systems.

similarity solution for the momentum equations. In contrast, the model presented here is statistical in nature and does not contain these simplifying assumptions of the previous model.

### 2.1. Conservation equations for the drops

*Drop number density equations.* For each initial-size class $j$ in the Eulerian coordinate system defined above, mass conservation is given by

$$\partial n_j/\partial t + [\partial(r n_j u_{drj})/\partial r]/r = 0, \quad [1]$$

where $n_j$ is the drop number density and $u_{drj}$ is the radial drop velocity including diffusive velocity. This equation holds between $r_{in,j}$ and $r_{out,j}$, respectively, the inner and outer radius of distribution $j$.

*Momentum equations.* We define the respective drop and gas angular momenta as $\Gamma_{d\theta j} = r_j u_{d\theta j}$ and $\Gamma_{G\theta} = r u_{G\theta}$ (here $\theta$ denotes azimuthal direction) so that the drop equations can be expressed as

$$\mathrm{d}r_j/\mathrm{d}t = u_{drj} \quad [2]$$

$$\mathrm{d}u_{drj}/\mathrm{d}t = [u_{d\theta j}]^2/r_j - v_{sj}[u_{drj} - u_{Gr}(r_j)] + \Lambda_{Tdj} + \Lambda_{pdj} \quad [3]$$

$$\mathrm{d}\Gamma_{d\theta j}/\mathrm{d}t = -v_{sj}[\Gamma_{d\theta j} - \Gamma_{G\theta}(r_j)], \quad [4]$$

where $v_{sj} \equiv \rho_G A_{dj} C_D \| \mathbf{u}_{sj} \| /(2m_{dj})$ is a rate associated with drag (cf. Bellan and Harstad 1990), $A_d$ is the drop transverse area, $C_D$ is the drag coefficient [assumed to have the same dependence upon $\mathrm{Re}_{dj}$ and evaporative blowing parameter as in Bellan and Harstad (1987) and Cliffe and Lever (1985)], $m_{dj}$ is the drop mass, and $\Lambda_{Tdj}$ and $\Lambda_{pdj}$ are body accelerations discussed below. The drag force here accounts for mean interactions among drops. Other force terms present in classical, single particle momentum equations (Hidy and Brock 1970; Maxey and Riley 1983) such as for example the Basset term, buoyancy term or the added mass term are here negligible.

*Energy equations.* To account for energy conservation within the drops and energy transfer to the gas adjacent to the drops, the 'sphere of influence' concept is modified to have a statistical significance. In the original definition of this concept [by Bellan and Cuffel (1983) for monodisperse, uniformly-distributed drop clusters] a fictitious sphere of influence was defined concentric with each drop in a cluster and having a radius $R_i$ equal to half the distance between the centers of two adjacent drops. Thus, the cluster volume consisted of the ensemble of spheres of influence and the interstitial space between them. This definition provided a geometric partition of the cluster volume, enabling an accounting of inter-drop interactions with the ratio of $R_i$ to the drop radius providing a quantitative measure of the cluster denseness (Harstad and Bellan 1991).

In the present work, we define $R_i$ statistically using

$$4\pi R_i^3 n/3 = PF, \quad [5]$$

where $n = \sum_{j=1}^{JT} n_j$ is the average total drop number density, $JT$ is the total number of initial-size classes, and $PF = 0.74$ is the packing factor (Bellan and Cuffel 1983).

With this definition, the class $j$ evaporation rate $\dot{m}_{dj}$ can be calculated for each $R_j$ using a previously derived model (Bellan and Harstad 1988). As in classical models (e.g. Williams 1965), the gas surrounding the drops is assumed quasi-steady with respect to the drops; however, unlike classical models, the gas density may be non-uniform. At the drop surface, the nonequilibrium process of evaporation is determined by the Langmuir–Knudsen kinetic law (Bellan and Harstad 1988). Unlike the previous interior drop model, the present model takes into account the effect on drop temperature profile of surface shear-induced circulation within the drop (using the effective-conduction correction of Abramzon and Sirignano 1989); details of the calculation of this profile are given in Harstad and Bellan (1991). Accordingly, the Ranz–Marshall correlation is not used and, instead, since $\mathrm{Re}_{dj} \leqslant O(10^2)$, the evaporation rate is multiplied by the laminar flow Nusselt number expression.

The $j$-class average gas temperature in the sphere of influence, $T_{Gj}$, must be known in order to calculate heat transfer to the drops and the evaporation rate. In the present model, $T_{Gj}$ is related to the edge gas temperature, $T_{Gi}$, via a polynomial involving $R_j/R_i$ (Bellan and Harstad 1988). In particular, $T_{Gi} = \xi_j T_{Gj}$, where i refers to the interstitial space between drops, $\xi_j = 1 + 2\lambda_j + 7\lambda_j^2$ and

$\lambda_j \equiv (1 - T_{Gsj}/T_G)R_j n^{1/3}$. Here $\lambda_j \ll 1$, $T_{Gsj}$ is the drop surface temperature for initial-size class $j$ and $T_G$ is the class-averaged gas temperature at given $r$. Similarly, $\rho_{Gi} = \rho_{Gj}/\xi_j$, where $\rho_G$ is the gas density. Averaging using the weights $n_j/n$ gives $T_{Gi} = \langle \xi_j \rangle T_G$, where $\langle \xi_j \rangle \simeq 1 + 2\langle \lambda_j \rangle + 4\langle \lambda_j \rangle^2 + 3\langle \lambda_j^2 \rangle$. These polynomial expressions result from a detailed consideration of averaging processes in the drop region.

### 2.2. Gas conservation equations

*Mass conservation*

$$\partial \rho_G/\partial t + [\partial(r\rho_G u_{Gr})/\partial r]/r = -\sum_j n_j \dot{m}_{dj}. \quad [6]$$

*Radial momentum conservation*

$$\rho_G(\partial u_{Gr}/\partial t + u_{Gr}\partial u_{Gr}/\partial r - u_{G\theta}^2/r) + \partial p/\partial r = F_{Gr}, \quad [7]$$

where $F_{Gr} = -\Sigma_j n_j(F_{drj} + \dot{m}_{dj}u_{srj})$ is the radial force on the gas and $F_{drj}$ is the radial force on the drops excluding turbulent effects. The expression for $F_{Gr}$ accounts for fluid dynamic gas-drop interaction and also for gas evaporated from the drops.

*Azimuthal momentum conservation*

$$\partial(\rho_G u_{G\theta})/\partial t + [\partial(r^2 \rho_G u_{Gr} u_{G\theta})/\partial r]/r^2 = \tilde{F}_{G\theta}, \quad [8]$$

where

$$\tilde{F}_{G\theta} = \sum_j n_j(v_{sj} m_{dj} u_{s\theta j} - \dot{m}_{dj} u_{d\theta j}) \quad [9]$$

is the azimuthal force on the gas and $u_{s\theta j}$ is the azimuthal component of $\mathbf{u}_{sj}$.

*Species conservation*

$$\partial(\rho_G Y_F)/\partial t + [\partial(r\rho_G u_{Gr} Y_F)/\partial r]/r = -\sum_j n_j \dot{m}_{dj} + \{\partial[D_T \rho_G r \partial Y_F/\partial r]/\partial r\}/r. \quad [10]$$

$Y_F$ is the gas mass fraction of the evaporating liquid component averaged over drop spheres of influence and $D_T$ is a turbulent mass diffusivity (modeled below).

*Energy conservation*

$$\partial(\rho_G h_G)/\partial t + [\partial(r\rho_G u_{Gr} h_G)/\partial r]/r = [\partial(rk_G \partial T_G/\partial r)/\partial r]/r + \sum_j n_j[\dot{m}_{dj}(\Delta h_{evap,j} - C_{pF} T_{Gsj} - 0.5u_{sj}^2) + v_{sj} m_{dj} u_{sj}^2], \quad [11]$$

where $h_G = C_{pG} T_G$ is the enthalpy, $\rho_G h_G = \gamma p/(\gamma - 1)$, $\gamma$ is the ratio of the heat capacities, $C_p$ is the specific heat capacity at constant pressure, $k_G$ is the conductivity, and $\Delta h_{evap}$ is the heat transferred to the drop from the gas per unit mass of evaporated fuel. The third and fourth terms on the right hand side of [11] show how incoming fuel vapor changes gas thermal and kinetic energies respectively while the last term gives viscous dissipation from drag.

*Equation of state.* The ideal gas law relates the pressure, temperature, density and mass fractions. Since the ambient pressure is assumed constant, other pressure contributions are small (see sections 2.5 and 5.1) and $C_{pG}$ is constant, it is seen that $\partial(\rho_G h_G)/\partial t \simeq 0$. Thus [11] becomes quasi-steady and determines $u_{Gr}$.

### 2.3. Discretization

Each initial-size class has associated Lagrangian radial coordinates $r_j^{(k)}(t)$, where $k$ identifies the discretization of the vortex into annular intervals $r_j^{(k)} < r < r_j^{(k+1)}$. All dependent quantities are

averaged over an interval as follows

$$\int_{r_j^{(k)}}^{r_j^{(k+1)}} V(r) r \, dr = 0.5\{[r_j^{(k+1)}]^2 - [r_j^{(k)}]^2\}\bar{V}, \quad [12]$$

where $\bar{V} = V[r_j^{(k+1.2)}] \equiv V^{(k+1.2)}$ and $r_j^{(k+1.2)} = \sqrt{0.5\{[r_j^{(k)}]^2 + [r_j^{(k+1)}]^2\}}$. Class $j$ drops in each radial interval have the same size and experience gas conditions at the edge of their sphere of influence determined by averaging over the radial interval and the drop classes.

The gas phase equations are solved using a coordinate system identified as $r_c^{(k)}$, which follows all drops in the cluster; this coordinate system will be determined in the discussion on dynamic drop-gas interaction below.

### 2.4. *Turbulence effects*

*Gas turbulence.* Within the vortex, it is assumed that small scale turbulence results from the azimuthal slip velocity between drops and gas; this assumption is inspired by the experimental evidence of Crowe *et al.* (1996) that particles enhance turbulence when their size is of same order as the gas turbulent length scale (see evaluation below). Because of its inherent complexity, a rigorous treatment of turbulence is impractical. Instead, following the traditional Prandtl 'mixing length' approach, the laminar viscosity is assumed enhanced by a turbulent contribution $\mu_T$ (cf. Schubauer and Tchen 1959), where $\mu_T = \rho_G A_T r_c \|\mathbf{u}_s\|$. Here $\mathbf{u}_s = \Sigma_j \mathbf{u}_{sj} N_{cj} / \Sigma_j N_{cj}$ is the mean slip velocity relative to the gas (the slip velocity appears because drop azimuthal motion generates small scale turbulent features as shown by order of magnitude estimates presented below), $N_{cj}$ is the $j$-class drop number in coordinates $r_c$, and $A_T \equiv C_T/\mathrm{Pr}_G$, where $\mathrm{Pr}_G$ is the gas Prandtl number and $C_T$ is a constant containing the uncertainty associated with a scaling approach (e.g. the mixing length model). The influence of $C_T$ upon the solution will be investigated to find the bounding behavior of turbulence.

$D_T$ is calculated from $D_T = (\mu_G + \mu_T)/(\rho_G \mathrm{Sc}_G)$ by prescribing the gas Schmidt number $\mathrm{Sc}_G$. Similarly, $k_G$ is calculated from $k_G = (\mu_G + \mu_T) C_{pG}/\mathrm{Pr}_G$ by prescribing $\mathrm{Pr}_G$. The gas Lewis number is taken to be unity ($\mathrm{Sc}_G = \mathrm{Pr}_G$), an accurate assumption for a gas.

*Drop turbulence.* The ratio of the Kolmogorov scale $\eta_K$ to $R_j$ is estimated from $\mathrm{Re}^{-0.75} R_c/R_j$ since $\eta_K/R_c = \mathrm{Re}^{-0.75}$. The characteristic flow velocity is $u_{G0} = 10^3$ cm/s. With $\mu_G = 4.2 \times 10^{-4}$ g/(cm s), $R_c = 2$ cm and $R_j = 2 \times 10^{-3}$ cm, one finds $\eta_K/R_j \sim O(1)$. Since $R_i/R_j \sim O(10)$ in the very dense configuration, many Kolmogorov-type eddies exist between adjacent drops. This not only supports the assumption regarding $\mu_T$, but also provides guidance for modelling how small turbulent scales affect drops. In analogy to Hidy and Brock (1970) who considered Brownian motion of particles induced by thermal fluctuations, we take into account how the fluctuations of small scale turbulent eddies (described using the mixing length approach) affect drop motion. Thus, the turbulent diffusion for drops is

$$D_{dTj} = A_T v_{sj} (r_j)^2 \quad [13]$$

which corresponds to the Stokes–Einstein formula with mean drop energy due to turbulence of $A_T m_{dj} (v_{sj} r_j)^2$. This mean drop energy corresponds to momentum fluctuations scaling as $\mu_G R_j r_j$ and may be compared to the Stokes limit small $\mathrm{Re}_{dj}$ drag that scales as $\mu_G R_j \mathbf{u}_{sj}$. Thus, the basic assumption here is that the characteristic velocity scales with cluster size. The change in radial velocity of a class $j$ drop due to the turbulent diffusion effect is assumed to be

$$\delta u_{drj} = -D_{dTj} \, \partial[\ln(n_j/n_j^0)]/\partial r, \quad [14]$$

where the superscript zero denotes the initial conditions. This means $\Lambda_{Tdj} = \delta(\mathrm{d}u_{drj}/\mathrm{d}t) = -D_{dTj} \, \mathrm{d}\{\partial[\ln(n_j/n_j^0)]/\partial r\}/\mathrm{d}t$ so that, using [1] to calculate $\mathrm{d}(\ln n_j)/\mathrm{d}t$, one finds

$$\Lambda_{Tdj} = D_{dTj}\{\partial\{[\partial(r u_{dj})/\partial r]/r\}/\partial r + \partial[\ln(n_j/n_j^0)]/\partial r \times \partial u_{drj}/\partial r\}. \quad [15]$$

### 2.5. *Pressure and dynamic drop-gas interaction modelling*

We consider the pressure to be the sum of several contributions all of which are modeled below.

*Large length scale drop-gas interaction.* The body force term $\Lambda_{pdj}$ in [3] describes drop-gas quasi-static interactions for length scales much larger than the drop radius whereas the term involving $v_{sj}$ accounts for drag resulting from small-scale pressure gradients. To understand the $\Lambda_{pdj}$ body force term, consider a drop located at $r_p$; the net radial force on the drop is $F_{ds} = -\int \hat{p}_n \cos\theta \, dA$, where $dA = 2\pi R^2 \sin\theta \, d\theta$ is the annular drop area element and $\hat{p}_n$ is the normal component of the large-scale pressure perturbation at the drop surface in a system of coordinates centered at the drop center. This large-scale perturbation arises from the non-local gas-drop interactions when there is a large number of drops. A Taylor expansion gives $\hat{p}_n \simeq \hat{p}(r_p) + (r - r_p)\partial\hat{p}(r_p)/\partial r$ and using $r - r_p = R\cos\theta$ gives $\Lambda_{pdj} = F_{ds}/m_d = -[4\pi R^3/(3m_d)]\partial\hat{p}/\partial r = -(1/\rho_L)\partial\hat{p}/\partial r$. The term $\partial\hat{p}/\partial r$ represents the volume gas force.

*Pressure effects due to centrifugal force on the gas.* Let $\tilde{p}$ be defined by $\partial\tilde{p}/\partial r = \rho_G u_{G\theta}^2/r$. The quantity $\partial\tilde{p}/\partial r$ varies as $M^2$, where $M$ is the Mach number. Although $\partial\tilde{p}/\partial r$ is generally small because $M \ll 1$, for small $r$ the contribution to $p$ from $\tilde{p}$ might be important because $u_{G\theta} \approx r^{-1}$ and the centrifugal force may be substantial at high vortex strength. With the boundary condition $\tilde{p}(r = R_c) = 0$, inside the cluster $\tilde{p}$ is given by

$$\tilde{p} = -\int_r^{r_{max}} \rho_G \Gamma_{G\theta}^2 \, dr/r^3. \qquad [16]$$

*Pressure change due to convection.* Let $p'$ be defined by $\partial p'/\partial r = -\rho_G(\partial u_{Gr}/\partial t + u_{Gr}\,\partial u_{Gr}/\partial r)$. For slow speed, quasi-steady flow, $p'$ satisfies Bernoulli's relation, $p' + \frac{1}{2}\rho_G u_{Gr}^2 = p_s(t)$. This approximation is acceptable here since $M \ll 1$ and does not affect the transient nature of the pressure, as shown below.

*Total pressure modelling.* For mathematical convenience, we define $p \equiv p'' + p_{amb} + \tilde{p} + p'$, where $p$ is the large scale pressure field and $p_{amb}$ is the ambient, constant pressure. According to the definitions of $F_{Gr}$, $\tilde{p}$ and $p'$, [7] becomes

$$\partial p''/\partial r = F_{Gr} = -\sum_{j=1}^{JT} n_j(F_{drj} + \dot{m}_{dj}u_{srj}). \qquad [17]$$

From [3] and the model for $\Lambda_{pdj}$,

$$F_{drj} = -m_{dj}[v_{sj}u_{srj} + (\partial\hat{p}/\partial r)/\rho_L]. \qquad [18]$$

By defining the liquid volume fraction $f_{vL} \equiv (\Sigma_j n_j m_{dj})/\rho_L$ and combining the above two equations one obtains

$$\partial p''/\partial r = F_{Gr} = \sum_{j=1}^{JT} n_j(v_{sj}m_{dj} - \dot{m}_{dj})u_{srj} + f_{vL}\,\partial\hat{p}/\partial r. \qquad [19]$$

Both $\tilde{p}$ and $p'$ are associated with flow dynamics and vary as $M^2$. In contrast, $\hat{p}$ is associated with a quasi-static interaction. Thus, it is reasonable to equate $p''$ and $\hat{p}$, giving

$$F_{Gr} = \partial\hat{p}/\partial r = \left[\sum_j n_j(v_{sj}m_{dj} - \dot{m}_{dj})u_{srj}\right]/(1 - f_{vL}). \qquad [20]$$

This equation is consistent with the physical situation and has the proper limiting behavior. Equation [20] shows that the volume force $F_{Gr}$ characterizes the effect of cluster 'porosity'. As $f_{vL} \to 1$, the cluster acts as one large liquid drop and the pressure gradient $\partial\hat{p}/\partial r$ becomes unbounded unless $u_{sr} \to 0$, thereby portraying the correct physics. From the definition of $p$ above, the quasi-steady approximation affects only $p'$, and the pressure term remains transient.

*Recasting of the conservation equations.* $r_c$ is defined through a velocity $u_{cr}$ such that $u_{cr}^{(k)} = dr_c^{(k)}/dt$, where $u_{cr}$ characterizes the radial motion of the cluster as an entity. It is also convenient to define the operator $\Delta_k$ by

$$\Delta_k V \equiv V^{(k)} - V^{(k-1)}$$

and

$$P_{G\theta}^{(k-1/2)} \equiv \int_{r_c^{(k-1)}}^{r_c^{(k)}} \rho_G \Gamma_{G\theta} r \, dr$$

which satisfies the relationship

$$\frac{d}{dt} P_{G\theta}^{(k-1/2)} = \int_{r_c^{(k-1)}}^{r_c^{(k)}} \tilde{F}_{G\theta} r^2 \, dr + \Delta_k [r \rho_G \Gamma_{G\theta} (u_{cr} - u_{Gr})] \qquad [21]$$

found by using [1], [8] and the definition of $\tilde{F}_{G\theta}$. Annulus-averaged gas mass and azimuthal momentum are defined as

$$M_G^{(k-1/2)} = \int_{r_c^{(k-1)}}^{r_c^{(k)}} \rho_G r \, dr$$

and

$$\bar{\Gamma}_{G\theta}^{(k-1/2)} = P_{G\theta}^{(k-1/2)} / M_G^{(k-1/2)},$$

where

$$\bar{\Gamma}_{G\theta}^{(k-1/2)} = r_c^{(k-1/2)} u_{G\theta}^{(k-1/2)}.$$

With these new notations [6], [9] and [21] yield the following conservation equation for $P_{G\theta}$

$$M_G^{(k-1/2)} \, d\bar{\Gamma}_{G\theta}^{(k-1/2)}/dt = \Delta_k [r \rho_G (u_{cr} - u_{Gr})(\Gamma_{G\theta} - \bar{\Gamma}_{G\theta}^{(k-1/2)}]$$

$$+ \int_{r_c^{(k-1)}}^{r_c^{(k)}} r \left[ \sum_j n_j (v_{sj} m_{dj} - \dot{m}_{dj})(\Gamma_{d\theta j} - \bar{\Gamma}_{G\theta}^{(k-1/2)}) \right] dr, \qquad [22]$$

where $u_{cr} = (\Sigma_j n_j m_{dj} u_{drj})/(\Sigma_j n_j m_{dj})$. In [22] the integral term gives the relaxation of angular momentum between gas and drops, while the difference term represents a source at the annulus boundaries. This source vanishes for irrotational (constant $\Gamma_{G\theta}$) flow.

### *2.6. Cluster boundary conditions*

Drop centrifugation results in the formation of a relatively thick drop shell inside the vortex. Thus, the cluster (formed by the drops and gas in that shell) exchanges mass, species, momentum and energy with the drop-free vortex regions in the vortex through an inner and an outer boundary. These boundaries are the statistical envelopes of the inner and outer drops as $R_{in} = \min_j(r_{in,j})$ and $R_c = \max_j(r_{out,j})$, where $r_{in,j}$ and $r_{out,j}$ are initially defined for all $j$s. Thus, space is partitioned into: (1) an inner drop-free region where the gas conservation equations are solved; (2) the cluster region where both gas and drop conservation equations are solved; and (3) the outer gas region where heat, mass and species satisfy convective–diffusive conservation equations.

The cluster appears to the surrounding gas as a porous material for which the drops represent the condensed phase. Thus, the surrounding gas cannot be easily engulfed by the cluster. Since the cluster does not have a solid boundary with the surrounding gas, there is limited shear at the cluster boundary and no exceptionally large velocity gradients are expected near the boundaries. However, relatively large gradients in the mass fractions and gas temperature may exist. Accordingly, the turbulent viscosity effect is included in the gas species equation through $Sc_G$ and in the gas energy equation through $Pr_G$, but no equivalent term exists in the gas momentum equation. Heat and species in the cluster surroundings are assumed to diffuse and convect towards the cluster from a prescribed value at infinity. In all our calculations there is no vapor of the evaporating compound in the far field and $T_{G\infty}(t) = T_{G\infty}^0[1 + t/(3 \times 10^{-2})]$ in order to simulate the passage of the vortex through an increasing temperature region; $T_{Gi}^0 = T_{G\infty}^0$.

If $u_{cr} > u_{Gr}$, the cluster engulfs gas at a rate proportional to $[r_c \rho_G (u_{cr} - u_{Gr})]_{r=R_c}$; if $u_{Gr} > u_{cr}$ the cluster emits gas and only weak diffusion couples it to the surrounding gas. Equivalent arguments

are valid for heat transfer. To model this situation, a Nusselt number approach is used where the correlation is $Nu_c = 1 + C_1 Pr_G Re_c$ and $Re_c = [\rho_G r_c \max(0, u_{cr} - u_{Gr})/(\mu_G + \mu_T)]_{r=R_c}$ is the effective Reynolds number. The power 1 is chosen for $Pr_G$ and $Re_c$ so that the expression for $Nu_c$ agrees for $C_1 = 1$ with the engulfing/emitting process described above. Constant $C_1$ is a free, phenomenological parameter whose influence upon the solution will be studied. Consistent with the similarity assumption $Sc_G = Pr_G$, the boundary condition for the evaporating species is

$$(r\,\partial Y_F/\partial r)_{r=R_c} = Nu_c(Y_{F\infty} - Y_{F,r=R_c}). \qquad [23]$$

At the inner cluster boundary, $\partial\Gamma/\partial r = 0$, where $\Gamma = Y_F$ or $\Gamma = T_{Gi}$. At the vortex center (taken to be an infinitesimally small radial distance to avoid singularities), the gradients of velocities and all dependent variables gradients vanish.

## 3. METHOD OF SOLUTION

The conservation equations are in Lagrangian frames except for the gas energy equation which is solved in an Eulerian frame as a radial difference equation. To solve the gas conservation equations, [6] and [10] are integrated over intervals in $r_c$ by evaluating the non-exactly-integrable term at $r_c^{(k+1/2)}$ similar to the definition of $r_j^{(k+1/2)}$. This yields equations for the time evolution of average gas and fuel vapor masses in the corresponding annuli. Equation [11] is similarly integrated except that it is steady because $M \ll 1$.

The number of class $j$ drops per unit vortex length in annulus $k$ is

$$N_j^{(k+1/2)} = 2\pi \int_{r_j^{(k)}}^{r_j^{(k+1)}} n_j r\, dr,$$

so [1] reduces to

$$dN_j^{(k+1/2)}/dt = 0.$$

The value of $p_{amb}$ is known and $\tilde{p}$ is calculated using [16], $p'$ is calculated from Bernoulli's relation, and $\hat{p}$ from [20]. The gas energy equation determines $u_{Gr}(t, r)$ and hence $u_s(t, r)$ while $T_G(t, r)$ is calculated from the equation of state. Further, $\rho_G(t, r)$ and $Y_F(t, r)$ are calculated from annular versions of [6] and [10], respectively; the values of $\bar{\Gamma}_{G\theta}$ determine $u_{G\theta}$; $r_j$ and constants $N_j^{(k+1/2)}$ determine $n_j$; $\Gamma_{d\theta j}$ is calculated from [4]; $r_j$ and $u_{drj}$ are calculated from [2] and [3], respectively. The drop internal temperature profile, $R_j$ and $\dot{m}_{dj}$ are calculated using previously developed models (Bellan and Harstad 1988; Harstad and Bellan 1991).

The system is solved as a set of first order nonlinear differential equations in time using piecewise linear interpolation procedures between the $r_c$ and $r_j$ coordinates to allow calculation of drop-dependent variables in the gas coordinate system. The algebraic solution procedure for the nonlinear drop equations requires iteration at each time step.

## 4. INITIAL CONDITIONS

Appendix A shows that an arbitrary initial distribution cannot be imposed for $u_{d\theta}$, $u_{d\theta}^0(r^0)$ because the Jacobian $J$ of the mapping $r^0 \to r$ may vanish causing the drop system of equations to become singular. A sufficient condition for the mapping to be regular is that the Jacobian be quasi-steady. This imposes the following constraint on $u_{d\theta}^0(r^0)$.

If $u_{dr}^0 = 0$, then $(dJ/dt)^0 = 0$; additionally $(d^2J/dt^2)^0 = 0$ if $(du_{dr}/dt)^0 = A^0$, where $A^0$ is constant. Therefore $u_{d\theta}^0(r^0)$ is determined through the momentum equation as

$$(u_{d\theta}^2/r)^0 = A^0 - v_s^0 u_{Gr}^0 \qquad [24]$$

$$u_{d\theta}^0 = \sqrt{r^0[A^0 - v_s^0 u_{Gr}^0(r^0)]} \qquad [25]$$

with $A^0 \geqslant v_s^0 \max(u_{Gr}^0)$.

Since $u_{d\theta}$ eventually relaxes to $u_{G\theta}$, it is still possible to generate a singularity at long times for certain choices of $u_{G\theta}^0(r^0)$. However, turbulent diffusion mitigates this effect, making a singularity avoidable. Thus, for each initial-size class, the initial drop radial acceleration, drop azimuthal

velocity, drop size, and drop temperature are prescribed as above. $u^0_{d\theta}$ may contain an additional term with respect to the expression in [25] for more complex situations than $(du_{dr}/dt)^0 = A^0$. This additional term is a drop cluster solid body rotation, $B^0_{d\theta}r^0$, which gives additional cluster expansion.

The initial number of drops per vortex length in class $j$ is

$$N^0_j \equiv 2\pi \int_{r^0_{in,j}}^{r^0_{out,j}} n^0_j r \, dr \qquad [26]$$

where $r^0_{in,j}$ and $r^0_{out,j}$ are the corresponding initial values of $r_{in,j}$ and $r_{out,j}$.

$n^0_j$ is defined from the value of $N^0_j$, and the radial distribution of the probability $\mathbf{p}_j(r)$ of finding a class $j$ drop at location $r$ as follows

$$n^0_j = N^0_j \mathbf{p}_j(r) \quad \text{for} \quad r^0_{in,j} \leqslant r \leqslant r^0_{out,j}. \qquad [27]$$

$\mathbf{p}_j(r)$ is measurable, but its value is sometimes uncertain as it depends upon instrument calibration (Presser *et al.* 1994). Here we chose a functional form that yields profiles consistent with observations (see below), while being general enough to allow the study of a myriad of profiles and so addresses the uncertainties in measurements; thus

$$\mathbf{p}_j(r) = A_{q_j}\eta^{q_j}e^{-q_j\eta} \qquad [28]$$

where $0 < q_j < \infty$ and

$$\eta_j \equiv (r - r_{in,j})/r_{q_j} \qquad [29]$$

so that $0 \leqslant \eta \leqslant \eta_{out,j}$ and

$$\max \mathbf{p}_j(r) = A_{q_j}e^{-q_j} \quad \text{at} \quad \eta_j = 1, \qquad [30]$$

where

$$r_{in,j} \equiv b_{ij}R^0_c, \quad 0 \leqslant b_{ij} \leqslant 1, \qquad [31]$$

$$r_{out,j} \equiv b_{oj}R^0_c, \quad b_{ij} < b_{oj} \leqslant 1, \qquad [32]$$

$$r_{q_j} \equiv \alpha_j(r_{out,j} - r_{in,j}), \quad 0 \leqslant \alpha_j \leqslant 1. \qquad [33]$$

$\eta_{out,j} = \alpha_j^{-1}$, and the maximum value of $n^0_j$ is located at a fraction $\alpha_j$ of distance from the inner edge ring to the outer edge. If $q_j \to 0$, then the distribution is uniform; if $q_j \gg 1$, the distribution is a sharp, Dirac delta function distribution. By requiring $2\pi\int_{r_{in,j}}^{r_{out,j}} \mathbf{p}_j(r) r \, dr = 1$ one finds

$$A_{q_j} = \left\{2\pi r_{q_j}\left[\frac{r_{in,j}}{q_j^{q_j+1}}\gamma\left(q_j+1, \frac{q_j}{\alpha_j}\right) + \frac{r_{q_j}}{q_j^{q_j+2}}\gamma\left(q_j+2, \frac{q_j}{\alpha_j}\right)\right]\right\}^{-1}, \qquad [34]$$

where $\gamma(a, b) \equiv \int_0^b t^{a-1}e^{-t}\,dt$.

$\mathbf{p}_j(r)$ provides the spatial dependence of $n^0_j$, whereas $N^0_j$, $\max_{r^0_j}(n^0_j)$, or the global initial air/liquid mass ratio $\Phi^0$ can be prescribed to yield an initial drop count.

Additional initial dependent variables to be prescribed are the gas pressure and temperature; cluster radius; irrotational component $A^0_{G\theta}$, and solid body rotation component $B^0_{G\theta}$ of the gas tangential velocity

$$u^0_{G\theta} = A^0_{G\theta}/r^0 + B^0_{G\theta}r^0 \qquad [35]$$

according to the findings of Nieh and Zhang (1992) that the tangential gas velocity in a strongly swirling vortex combustor exhibits a Rankine type of vortex flow. $u^0_{Gr}$ is calculated from [11].

The initial properties of gas (air) and liquid are also prescribed. Constants $C_T$ and $C_l$ are considered parameters of the problem.

Table 1. Thermophysical properties used in the calculations

| $n$-Decane | Air |
|---|---|
| Heat capacity of liquid $C_{pL} = 0.523$ cal/(g°K) | $C_{pa} = 0.241$ cal/(g°K) |
| Liquid density $\rho_L = 0.734$ g/cm$^3$ | $W_{aG} = 28.9$ g/mole |
| Liquid conductivity $k_L = 2.5 \times 10^{-4}$ cal/(cm°K s) | $\mu_{G\infty} = 4.2 \times 10^{-4}$ g/(cm s) at 1000° K |
| Liquid viscosity $\mu_L = 2.6 \times 10^{-2}$ g/(cm s) | $Pr_G = 0.8$ |
| Liquid diffusivity $D_{mL} = 4 \times 10^{-5}$ cm$^2$/s | |
| Latent heat of evaporation $L_{evap} = 73.92$ cal/g | |
| Heat capacity of vapor $C_{pvap} = 0.4$ cal/(g°K) | |
| Normal boiling point temperature $T_b = 447.7$°K | |
| Molecular weight $W = 142$ g/mole | |

$\Delta C_p = C_{pL} - C_{pG} = 0.0292$ cal/(g°K), fitted for the saturation pressure curve.

## 5. RESULTS

### 5.1. *Baseline behavior*

Due to the large number of parameters (table 1), for reference a baseline calculation was performed, consistent with previous results (Bellan and Harstad 1990) for monodisperse, uniformly distributed drop clusters in vortical flows. These results indicated that very dense sprays have $R_i/R \leqslant 10$, dense sprays have $10 < R_i/R < 15$, moderately dense sprays have $15 < R_i/R < 30$, and dilute sprays have $R_i/R \geqslant 30$. For $n$-decane it was found (Bellan and Harstad 1990) that for $\Phi^0 = 0.314$ (stoichiometric is 15.0) the cluster was dense, for $\Phi^0 = 0.785$ the cluster was moderately dense, while for $\Phi^0 = 1.57$ the cluster was on the borderline between moderately dense and dilute. In the present model $n$ need not be uniform and the initial drop size is not monodisperse so, depending upon the $n^0$ profile, a global $\Phi^0 = 0.314$ may simultaneously involve very dense, moderately dense and dilute regions.

The drop sizes chosen here are relevant to gas turbine engines, Diesel engines, furnaces and medical sprays. The initial conditions for the velocities are chosen only for illustrative purposes. The initial gas and drop temperatures are relevant to a variety of combustion systems. For $\alpha_j$ and $q_j$ chosen as in figure 2 caption, the initial distribution is dense, except for the inner part of the cluster, allowing meaningful comparisons with previous results. Because the ratio plotted is an average, the drops of a given $j$-class might be in a denser or more dilute configuration depending upon the specification of $\max_{r_j^0}(n_j^0)$ for each initial-size class.

Figure 3, the dependence of $n$ on $r_c$, shows that the initial profile evolves into an increasing function of $r_c$ except at the cluster's outer boundary region. The drop-free innermost region of the cluster expands as drops centrifuge to outer vortex portions. In this inner region, smaller

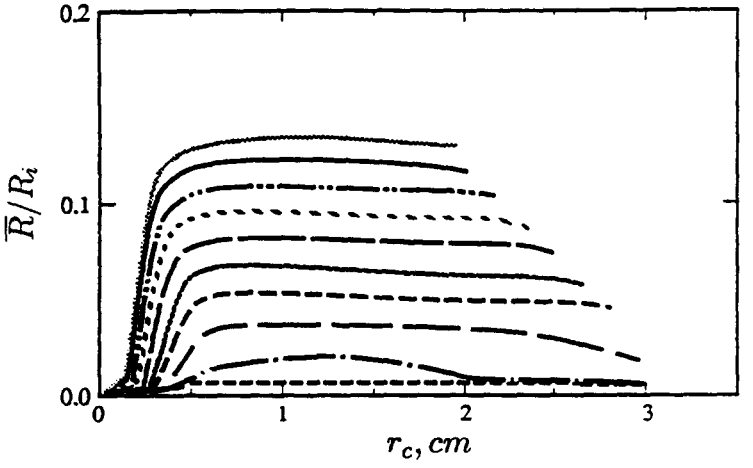


Figure 2. Ratio of the average drop diameter by the average distance between the centers of two adjacent drops versus the coordinate associated with the gas in the cluster at different times. Initial parameters are: $\Phi^0 = 0.314$, $T_{G1}^0 = 1000$° K, $T_{G5}^0 = 350$° K, $R_1^0 = 2 \times 10^{-3}$ cm, $R_2^0 = 2.5 \times 10^{-3}$ cm, $\max_{r_2^0}(n_2^0)/\max_{r_1^0}(n_1^0) = 1/3$, $\alpha_1 = \alpha_2 = 0.5$, $q_1 = q_2 = 0.5$, $R_c^0 = 2$ cm, $b_{i1} = b_{i2} = 0.1$, initial drop acceleration for both classes is 20 cm/s$^2$, null initial drop spin rate for both initial-size classes, $u_{G\theta}^0 = 100/r_c$ cm/s, $C_T = 5 \times 10^{-2}$, $C_1 = 0.35$. Refer to table 2 for the legend.

Table 2.

| Line symbol | Time, s |
|---|---|
| ——————— | $6.99 \times 10^{-5}$ |
| ——————— | $7.69 \times 10^{-4}$ |
| — - - — - - — - - — | $1.47 \times 10^{-3}$ |
| - - - - - - - - - - - - - - - - - | $2.17 \times 10^{-3}$ |
| — — — — — — | $2.87 \times 10^{-3}$ |
| ——————— | $3.56 \times 10^{-3}$ |
| — — — — — — — — | $4.26 \times 10^{-3}$ |
| - — — — — — — - | $5.66 \times 10^{-3}$ |
| — - - - - — - - - — | $7.06 \times 10^{-3}$ |
| - - - - - - - - - - - - - | $8.39 \times 10^{-3}$ |

initial-size-class-1 drops dominate initially and remain for longer times as shown in figure 3(b) and (c). Although initial-size-class-1 drops dominate the outer edge at first, as the calculation proceeds and the cluster expands, the initially larger initial-size-class-2 drops are centrifuged further out. Since in the same surroundings their evaporation rate is slower because of their larger thermal inertia time, they remain larger and are centrifuged further. Initial-size-class-1 drops dominate the central part of the vortex throughout the calculation. Similar variations of $n$, peaked initially at the mean location in the annulus of a swirling pressure-atomized burning spray, were observed by Gupta *et al.* (1996). In those observations, the peak was decreasing with downstream axial location, which in our axisymmetric configuration would correspond to an evolution in time. The central core region of the spray devoid of drops became enlarged with axial position, similar to our predicted time evolution. Aftel *et al.* (1996) found similar variations of $n$ with radial distance for swirling sprays produced by an air-assist atomizer. For both constant mass flow and constant momentum flow, and for all types of atomizing gas, the profiles display a maximum in the mean part of the annulus, relaxing with increasing axial distance in a similar manner to our predicted temporal relaxation.

Figure 4 shows the size distribution of the two initial-size classes within the cluster at different times and demonstrates that each initial-size class develops its own size distribution. Drops at the cluster periphery are in contact with hotter gas and evaporate faster, whereas drops located near the mean cluster radius are in contact with colder gas and evaporate slower (see figure 5). The lower gas temperature in this part of the cluster is attributed to the higher value of $n^0$ since the heat required to evaporate more drops represents an increased heat sink for the gas. The larger gas temperature at the outer cluster periphery is due to the continuous flux of hot gas encountered as the cluster expands into hotter surroundings. The larger gas temperature at the inner cluster periphery results from centrifugally-induced drop depletion. In the absence of drops, the gas has no heat sink and its temperature remains near the initial value. A sharp temperature gradient develops as $r_c$ increases, corresponding to the increase in $n$. The nonmonotonic behavior for $r_c < 1$ cm is attributed to different contributions to $n$ from the two initial-size classes. $n$ is a monotonically increasing function of $r_c$ within the mean region of the cluster; however, the $n_2$ profile develops a slight minimum within the mean region of the cluster. This slight minimum corresponds to the slight local maximum in the temperature profile since there is a decreasing heat sink on the gas. This slight local temperature maximum impacts evaporation and figure 4(b) shows the evolution of a slight dip occurring for $r_c$ slightly smaller than 1 cm.

Measurements of the Sauter mean diameter ($D_{32} = [\Sigma_{j=1}^{JT} n_j (2R_j)^3]/[\Sigma_{j=1}^{JT} n_j (2R_j)^2]$) in sprays reveals behavior similar to our calculations. Presser *et al.* (1986) found that in swirling isothermal hollow cone sprays, $D_{32}$ reached a minimum at $r = 0$ and peaked in the mean part of the annulus; the value of $D_{32}$ at the outer edge of the spray was higher than at $r = 0$, also in agreement with our predictions. Our values at the outer cluster boundary are relatively lower with respect to those at the inner cluster boundary than in the experiments because in our calculations the cluster encounters regions of larger surrounding temperature as a function of time whereas in the experiments the surrounding gas has the same temperature as a function of axial distance. The axial evolution of the measured profiles shows decreasing $D_{32}$ values corresponding to the time evolution of our calculations. McDonell *et al.* (1992) measured $D_{32}$ as well as $D_{10} = \Sigma_{j=1}^{JT} n_j (2R_j)/n$ for both reacting and non reacting swirling air-assist sprays and showed similar results to Presser *et al.*'s

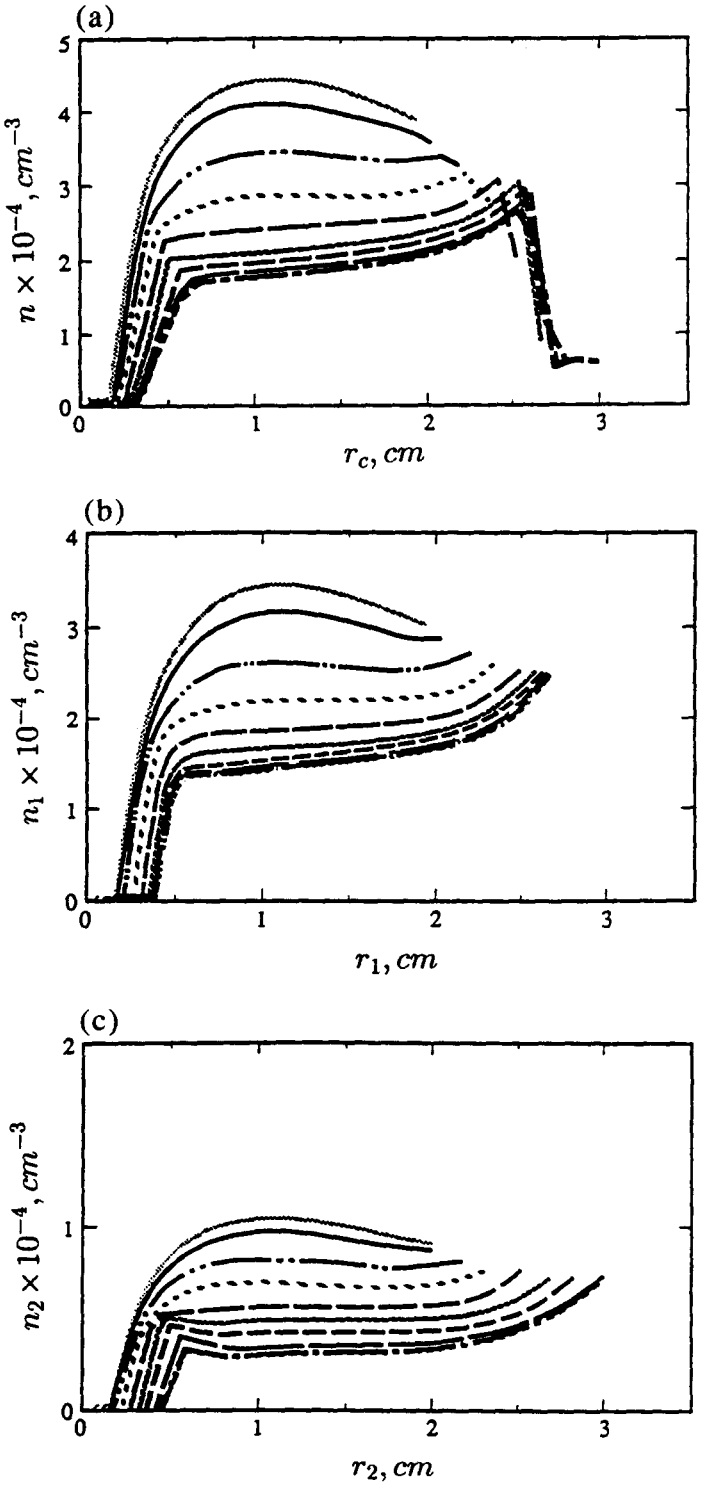


Figure 3. Total drop number density (a), drop number density of initial-size-class-1, (b) and drop number density of initial-size-class-2 (c) vs the radial coordinate in the cluster at various times. Initial conditions and parameters are listed in the figure 2 caption. Refer to table 2 for the legend.

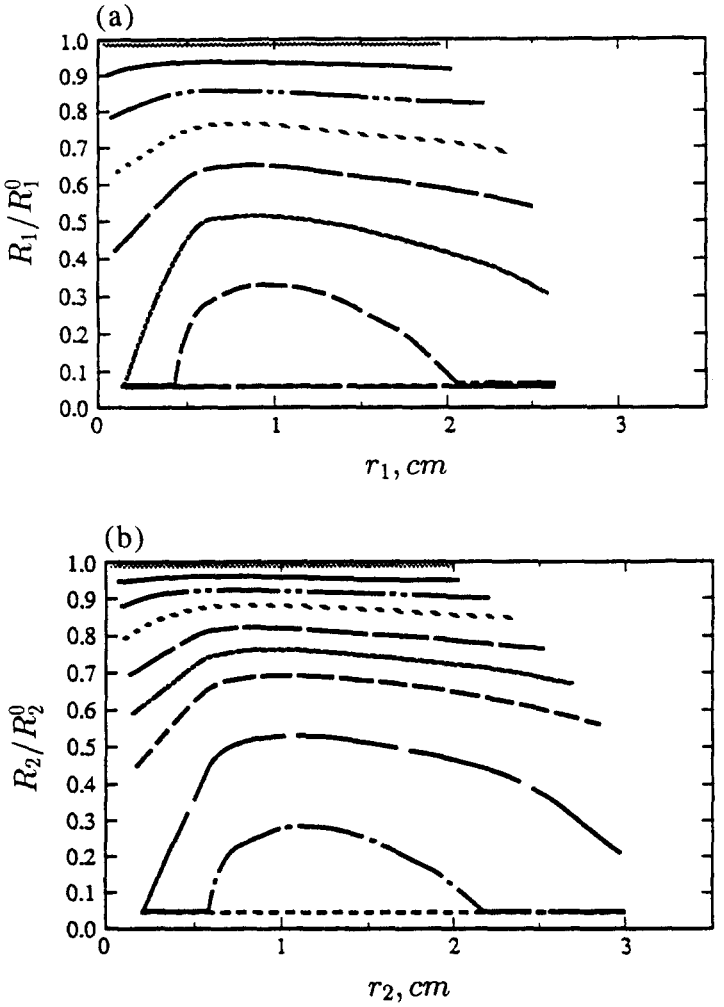


Figure 4. Residual drop radius for initial-size-class-1 (a) and initial-size-class-2 (b) vs the radial coordinate in the cluster at various times. Initial conditions and parameters are listed in the figure 2 caption. Refer to table 2 for the legend.

(1986) except that in McDonell *et al.* (1992) the profiles continue to increase with radial distance up to the edge of the spray; obviously, the boundary conditions at the edge of the spray play a major role in determining these values. Data from the experiment showed the formation of an enlarged core as a function of the axial position where both $D_{32}$ and $D_{10}$ reached minima, which is in qualitative agreement with our results.

The $n$ and $n_j$ evolution is elucidated from the drop tangential velocities and the angle between the velocity vector and the tangential coordinate. The tangential velocities exhibit a minimum at a location close to the inner cluster periphery whereas the velocity angle exhibits a maximum at the same location; this maximum decreases with time and shifts towards larger $r_c$. The minimum tangential velocity causes accumulation of drops and the resulting sharp increase in $n$ near the inner cluster periphery. The velocity angle is affected by both tangential motion and particle centrifugation. As time increases, the largest centrifugation shifts from the inner cluster periphery to the central vortex region.

Figure 6 illustrates the development of $Y_F$ vs $r_c$. For small times the profile is asymmetric with respect to the mean radial location in the cluster. The smaller value of $Y_F$, both at the inner and outer cluster periphery, corresponds to regions of low $n$. At large times, the profiles become almost symmetric with respect to the mean radial location in the cluster and the mean evolves almost into a plateau. The low $Y_F$ values at the inner and outer cluster peripheries still correspond to the regions

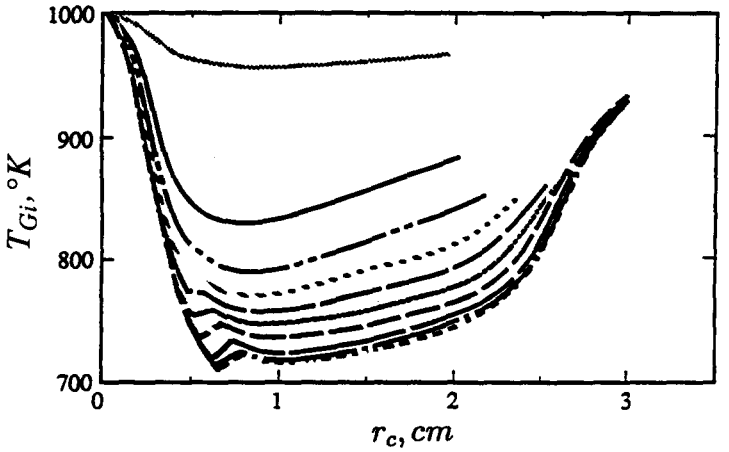


Figure 5. Interstitial gas temperature in the cluster versus the radial coordinate in the cluster at different times. Initial conditions and parameters are listed in the figure 2 caption. Refer to table 2 for the legend.

of low $n$. The sharp edge between the inner cluster periphery and the mean plateau corresponds to the sharp edge of $n$ at the same location.

*5.2. Effect of the air/fuel mass ratio, $\Phi^0$*

Results from calculations performed with $\Phi^0$ of 0.785 and 0.157 are compared with those obtained with $\Phi^0 = 0.314$ in figures 7–13. All other values of initial conditions and parameters remain the same (see figure 2 caption).

Figure 7 shows the ratio of the average drop radius to the sphere of influence radius, giving an indication of the cluster density. Denser clusters contain more mass and thus the centrifugal force is larger. Figure 8 depicts $n$ vs $r_c$ for the three different calculations at the same times and shows that denser clusters are centrifuged further out. When the cluster is initially more dilute, $n$ becomes more uniform inside the cluster (except at the inner and outer peripheries of the cluster), a consequence of the change in the drop velocity profiles. Figure 9 shows that the drop radial velocity in a more dilute cluster is larger in the inner part than in the outer part; the opposite occurs in a denser cluster. Figure 10 shows a similar change in behavior for $u_{d\theta}$ with an additional development of a more uniform profile in the central and outer part of the cluster. The drag force and evaporation rate strongly couple the velocity and $n$ profiles, making it impossible to determine cause and effect. The results in figure 8 validate the uniform $n$ assumption for dilute drop clusters, but for dense drop clusters this assumption seems unrealistic.

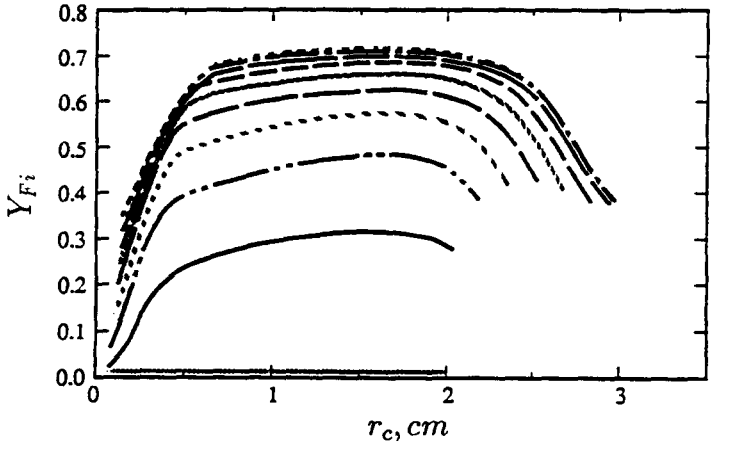


Figure 6. Interstitial mass fraction of the evaporated compound in the cluster versus the radial coordinate at various times. Initial conditions and parameters are listed in the figure 2 caption. Refer to table 2 for the legend.

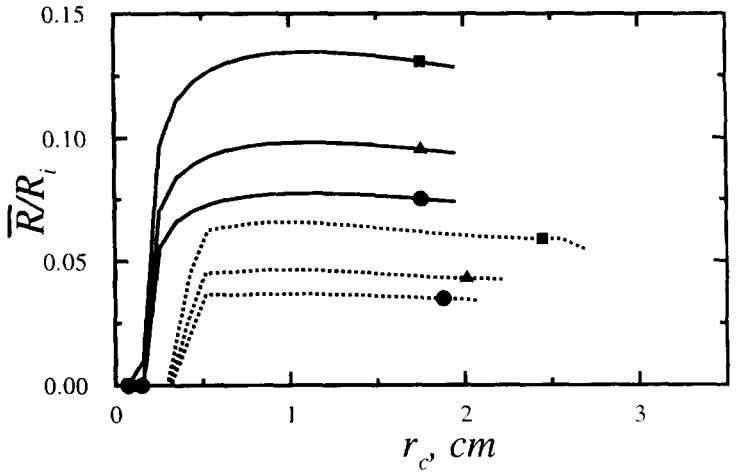


Figure 7. Ratio of the average drop diameter by the average distance between the centers of two adjacent drop diameters vs the radial coordinate at $7 \times 10^{-5}$ s (solid lines) and $3.56 \times 10^{-3}$ s (dotted lines) for $\Phi^0 = 0.314$ (■), 0.785 (▲), 1.57 (●).

Mean radial velocities as a function of the radial position were measured by Presser *et al.* (1986), Gupta *et al.* (1996) and McDonell *et al.* (1992). In all these experiments, the mean radial velocity increased with $r$, exhibited a peak and further decreased to the edge of the spray. In the experiments of McDonell *et al.* (1993), the mean radial velocity, plotted for temporal (not initial) size-classes, either exhibited a local maximum near the axis, had a slight minimum and then increased further with $r$, or was an increasing function of $r$. Our predictions are consistent with these experimental observations. The decay with axial distance observed in the experiments is consistent with the temporal decay of our predictions.

Mean azimuthal velocities were measured by McDonell *et al.* (1992) and show the same variation as our predictions: a maximum close to $r = 0$, then a dip followed by a further increase as a function of $r$ and the eventual reaching of a plateau with increasing axial position duplicating our temporal predictions. The relaxation of the profiles with axial distance in the data again validates our predicted temporal relaxation. The qualitative agreement of our radial and azimuthal velocity predictions with data indicates that the two-way dynamic coupling of drops and flow is modeled correctly.

Figure 11 shows $T_{Gi}$ vs $r_c$ for three selected times and three values of $\Phi^0$. When the gas temperature exceeds the initial drop temperature, a denser drop cluster provides a greater heat sink for the gas, resulting in much lower temperatures at the cluster center. Radial variation of the mean

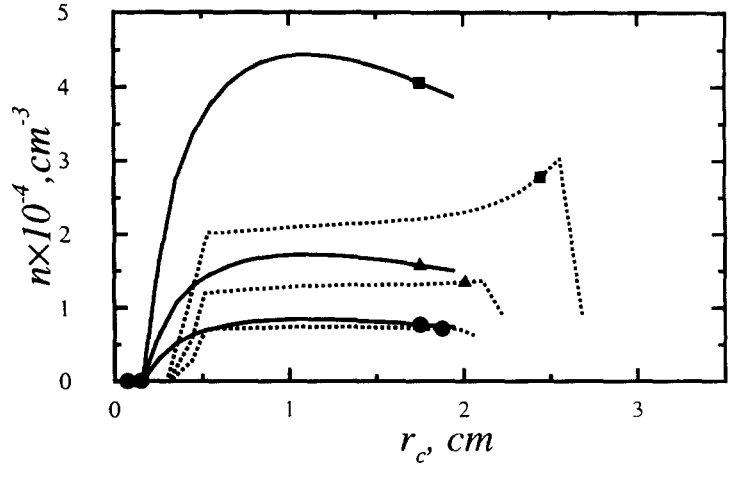


Figure 8. Total drop number density vs the radial coordinate at $7 \times 10^{-5}$ s (solid lines) and $3.56 \times 10^{-3}$ s (dotted lines) for $\Phi^0 = 0.314$ (■), 0.785 (▲), 1.57 (●).

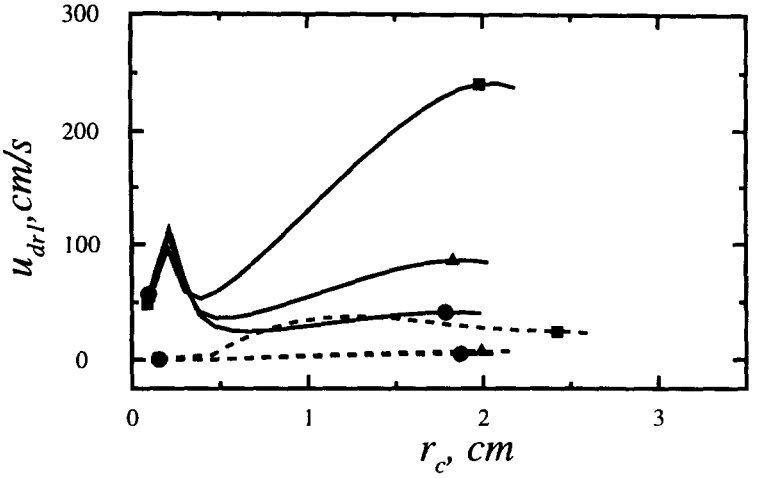


Figure 9. Radial drop velocity for initial-size-class-1 vs the radial coordinate at $7 \times 10^{-5}$ s (solid lines) and $3.56 \times 10^{-3}$ s (dotted lines) for $\Phi^0 = 0.314$ (■), 0.785 (▲), 1.57 (●).

temperature measured by Presser and Semerjian (1988) for swirling air-assist sprays showed that profiles are a strong function of the atomization air flow rate. For low flow rates and close to the atomizer, the temperature decreases from the centerline to a minimum, further increases to a maximum and decays to the edge of the spray. At further axial positions, the temperature increases from the centerline to a peak that is located to increasing radial positions as the axial distance increases, and finally decays to the spray edge. These profiles are typical of hollow cone sprays. For high atomization flow rates, in the near field of the atomizer the temperature decreases from a maximum on the centerline to a local minimum in the mean part of the spray annulus, increases again and finally decays at the edge of the spray. In the far field, the temperature profile forms a plateau from the centerline to a radial position increasing with axial distance, and finally decreases to the edge of the spray. According to the authors, this profile is indicative of an inner and outer flame sheet. The predictions displayed in figure 11 compare qualitatively very well with the high atomization flow rate situation, except that at the outer cluster edge the temperature remains large due to the simulated passage of the cluster through regions of increasing surrounding temperature. The qualitative agreement of the mean temperature in the near field and the above discussion on $D_{32}$ and $D_{10}$ indicate that the thermodynamic and thermophysical coupling of drops and flow are correct.

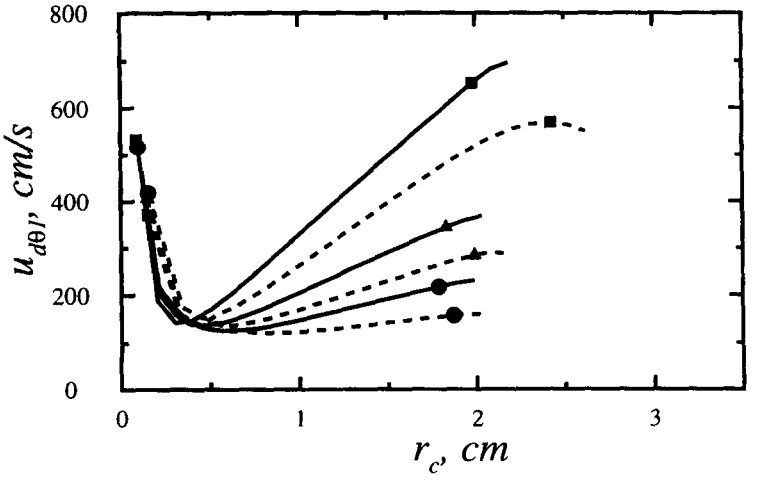


Figure 10. Tangential drop velocity for initial-size-class-1 vs the radial coordinate at $7 \times 10^{-5}$ s (solid lines) and $3.56 \times 10^{-3}$ s (dotted lines) for $\Phi^0 = 0.314$ (■), 0.785 (▲), 1.57 (●).

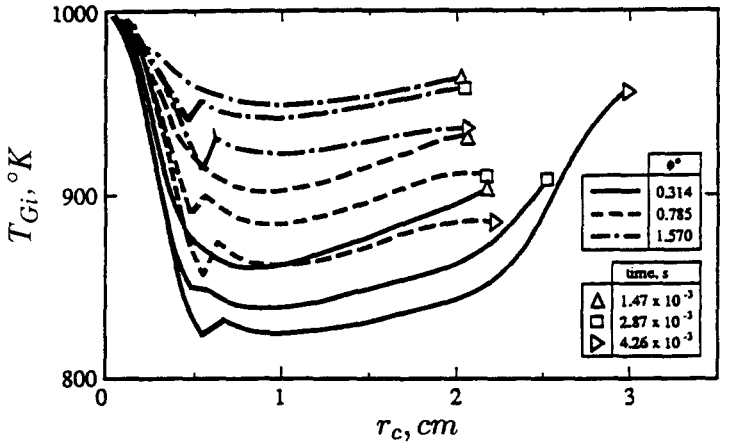


Figure 11. Development of the interstitial gas temperature profile for $\Phi^0 = 0.314$, 0.785 and 1.57. All other initial conditions and parameters are listed in the figure 2 caption.

Figure 12 shows the radial variation of the residual drop radius for initial-size-class-1, $R_1/R_1^0$, at various times, indicating the result of the interaction between drops and gas. The drops in denser clusters take considerably longer to evaporate and the drop size distribution is substantially more nonuniform. This is because the drop competition for heat results in a slower heating rate, and heat transported from the cluster boundaries towards the interior has greater difficulty reaching the cluster center than when the cluster is dilute. Our predictions show that the situation is exacerbated for the initially larger drops (not illustrated).

Both $n$ and the evaporation rate control the distribution of $Y_F$. Figure 13 shows that when the cluster is initially denser, the maximum value of $Y_F$ is larger and the distribution is more symmetric with respect to the mean location in the cluster. The last effect is attributed to the greater centrifugation which (differentially) brings drops to the outer cluster boundary.

### 5.3. *Influence of the initial drop size distribution at fixed* $\Phi^0$

Calculations were performed for monodisperse initial drop size distributions (the simplest case) for $\Phi^0 = 0.314$ with $R^0 = 2 \times 10^{-3}$ cm. The nondimensional radius of the sphere of influence is exactly the same as in the typical calculations described in 5.1, but $n^0$ is much larger (see figure 14) than in the bimodal initial distribution of the baseline calculation because the liquid mass is the same but there is a substantial number of smaller drops. Since the drops are smaller on average, centrifugation effects are reduced and the drops penetrate the hot surroundings less. Thus, the gas

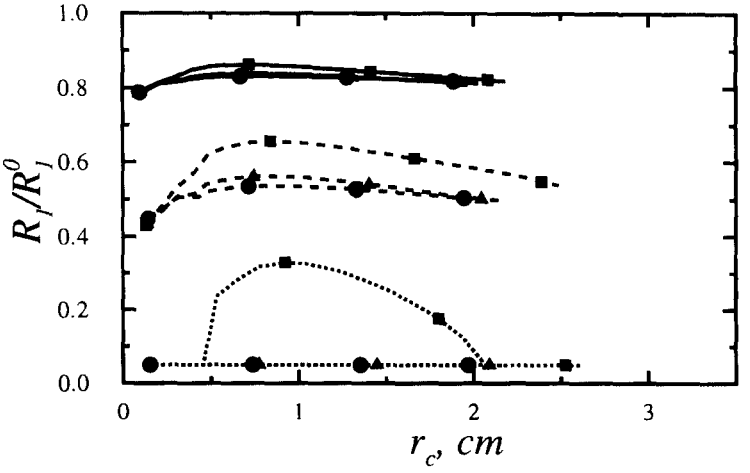


Figure 12. Residual drop radius for initial-size-class-1 vs the radial coordinate at $7 \times 10^{-5}$ s (solid lines), $2.87 \times 10^{-3}$ s (dashed lines) and $3.56 \times 10^{-3}$ s (dotted lines) for $\Phi^0 = 0.314$ (■), 0.785 (▲), 1.57 (●).

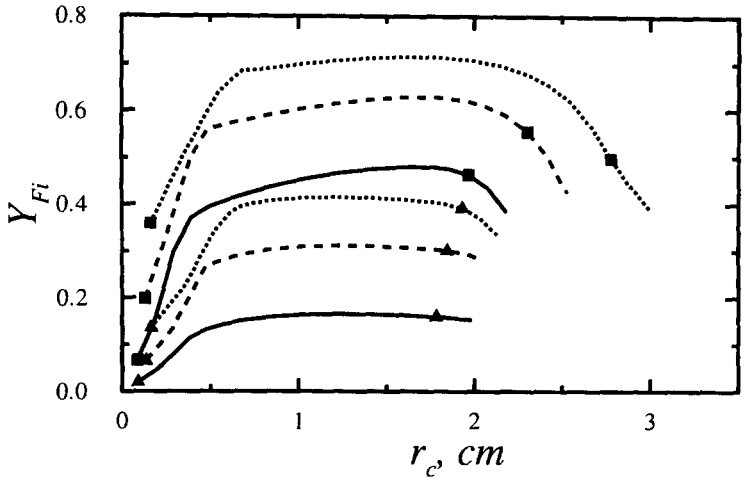


Figure 13. Mass fraction of the evaporated compound at $1.44 \times 10^{-3}$ s (solid lines), $2.87 \times 10^{-3}$ s (dashed lines) and $4.26 \times 10^{-3}$ s (dotted lines) for $\Phi^0 = 0.314$ (■) and 1.57 (▲).

temperature distribution is almost identical to that of the baseline calculation, except for the outer third of the cluster where it is substantially lower. Drops located in the outer half of the cluster experience a slightly reduced evaporation rate towards the end of their lifetime. Dynamics and evaporation are thus controlled by $\Phi^0$ in the inner half of the cluster and by $n^0$ in the outer half. The persistent strong nonuniformity in $n$ and the quickly-evolving nonuniformity in $R$ during the early part of the calculation in the inner part of the cluster are both noteworthy. For example, when $t = 3.56 \times 10^{-3}$ s, at the inner cluster boundary $R/R^0(r_c = 0.12\text{ cm}) = 5 \times 10^{-2}$, whereas $R/R^0(r_c = 0.8\text{ cm}) = 5.2 \times 10^{-1}$.

The evolution of an initially uniform drop number density having a monodisperse size distribution is an important theoretical issue. Calculations were performed for this case using $R^0 = 2 \times 10^{-3}$ cm and $\Phi^0 = 0.314$ ($q = 10^{-3}$ to give uniform $n^0$). The results in figure 14 show that except for the outer and inner portions of the cluster (20% and 10% of the radial span, respectively), $n$ remains uniform. Even if $n$ is uniform, neither the $T_{Gi}$ distribution nor $R/R^0$ stay uniform indicating that the heat transfer characteristic time exceeds the drop lifetime. Thus, the drops at the cluster periphery effectively 'screen' the heat, and only heat not absorbed by the drops at the cluster edges penetrates to the cluster's central region. In the cluster's central region, the gas temperature is considerably lower than at the periphery because the drops extract substantial heat from the gas due to the temperature difference and this heat does not get replenished. For example,

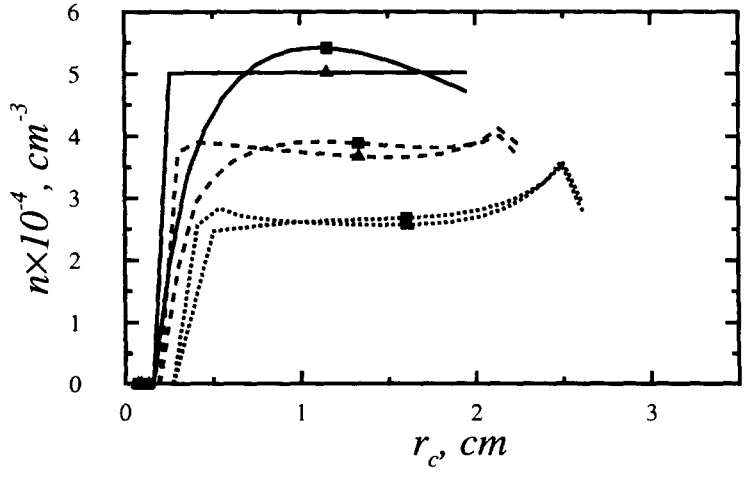


Figure 14. Drop number density at $7 \times 10^{-5}$ s (solid lines), $1.47 \times 10^{-3}$ s (dashed lines) and $2.87 \times 10^{-3}$ s (dotted lines) for two monodisperse size distributions ($R^0 = 2.0 \times 10^{-3}$ cm). Initially, one drop number density is uniform (▲) and the other has the parameters given in the figure 2 caption (■).

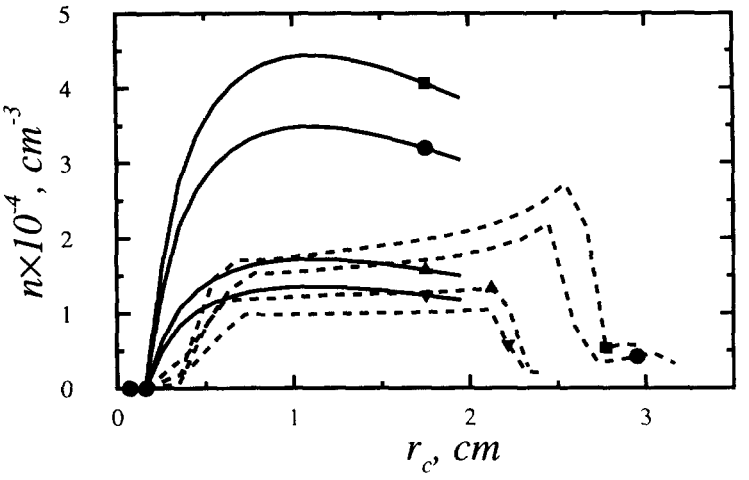


Figure 15. Total drop number density vs radial position at $7 \times 10^{-5}$ s (solid lines) and $8.4 \times 10^{-3}$ s (dashed lines) for bimodal size distributions with $\Phi^0 = 0.314$ and $R_2^0 = 2.5 \times 10^{-3}$ cm (■); 0.785 and $R_2^0 = 2.5 \times 10^{-3}$ cm (▲); 0.314 and $R_2^0 = 3.0 \times 10^{-3}$ cm (●); 0.785 and $R_2^0 = 3.0 \times 10^{-3}$ cm (▼). All other initial conditions and parameters are listed in the figure 2 caption.

when $t = 3.56 \times 10^{-3}$ s, the maximum $R/R^0$ is 0.52, whereas the drops at the inner edge of the cluster have completely evaporated and $R/R^0$ at the outer cluster edge is 0.31. Comparison with Bellan and Harstad (1990) indicates that if $n^0$ is uniform, $n$ will stay uniform throughout most of the cluster, but the initial uniformity of the drop size distribution is not maintained.

The effect of changing one of the drop sizes of an initial bimodal distribution was investigated for $\Phi^0 = 0.314$ and for $\Phi^0 = 0.785$. In both cases, now $R_2^0 = 3.0 \times 10^{-3}$ cm, instead of $R_2^0 = 2.5 \times 10^{-3}$ cm. When $R_2^0$ is larger, $n^0$ is smaller (because the initial total mass is the same), and centrifugation effects eventually become more important. However, when $\Phi^0 = 0.785$ there is less liquid mass than when $\Phi^0 = 0.314$, and so centrifugation effects become less important. A comparison of the $n$ profiles for the two values of $\Phi^0$ and the two bimodal distributions appears in figure 15. When $R_2^0 = 3.0 \times 10^{-3}$ cm, the drops remaining at the outer cluster periphery at the end of the calculation are large drops from initial-size-class-2 that have not completely evaporated. Since $\max_{r_1^0} n_1^0 / \max_{r_2^0} n_2^0$ is the same as in the previous calculations, $n_1^0$ is now smaller than in the baseline calculation; this is why drops in initial-size-class-1 evaporate at approximately the same rate as in the baseline calculation (section 5.1), while being centrifuged slightly less. The small increase in the evaporation rate of drops in the outer half of the cluster is attributed to the fact that initial-size-class-2 eventually expands the cluster further and allows more heat to penetrate the cluster. This interpretation is supported by the fact that the ultimate $T_{Gi}$ is substantially higher at the cluster edge when initial-size-class-2 consists of larger drops. At early times, when $R_2^0$ is smaller, the larger value of $n$ promotes a stronger drop-gas interaction. As the drops are centrifuged, they entrain gas, increasing $u_{Gr}$; the cluster expands further, encountering larger gas temperatures which promote heat transfer and result in a larger gas temperature at the outer cluster edge.

Centrifugation of these larger drops also disperses vapor very effectively into the surroundings; although the maximum value of $Y_F$ is slightly lower when the drops in initial-size-class-2 are larger, vapor penetration into the surroundings is more effective. This physical picture agrees with the well established fact in spray combustion that the small drops in a spray are responsible for spray ignition, whereas the fuel vapor produced by the larger drops is responsible for flame propagation.

All these effects are greatly reduced when $\Phi^0 = 0.785$ instead of $\Phi^0 = 0.314$, indicating that the dense regions of a spray contain more control parameters than the dilute regions. Thus, any spray optimization process is more likely to be successful if initiated in the dense spray region near the atomizer.

At a fixed time, larger maximum $Y_F$ is obtained for given $\Phi^0$ when $R_2^0$ is smaller, whereas larger vapor penetration into the ambient is obtained when $R_2^0$ is larger. The question then arises whether the evolution of an initial trimodal distribution can combine these characteristics, both of which are desirable for the combustion of atomized liquid fuel. Figure 16 illustrates $T_{Gi}$ and $Y_F$ obtained

with a trimodal distribution when $R_1^0 = 2 \times 10^{-3}$ cm, $R_2^0 = 2.5 \times 10^{-3}$ cm and $R_3^0 = 3 \times 10^{-3}$ cm with $\max_{r_3^0}(n_3^0) = 0.5 \max_{r_2^0}(n_2^0)$ and $\Phi^0 = 0.314$; the evolution of the trimodal $T_{Gi}$ and $Y_F$ are being compared to the two bimodal ones, one having the largest initial-size class $R_2^0 = 2.5 \times 10^{-3}$ cm and the other having $R_2^0 = 3 \times 10^{-3}$ cm. The differential centrifugation/evaporation according to the initial-size class causes the cluster to penetrate more into the surroundings than did a bimodal distribution cluster with $R_2^0 = 2.5 \times 10^{-3}$ cm (compare figure 16 with figures 5 and 6). Comparisons of the maximum $Y_F$ attained show that it is larger with the trimodal distribution than with the bimodal distribution having $R_2^0 = 3 \times 10^{-3}$ cm (not illustrated). Notably, the trimodal $T_{Gi}$ at the outer cluster edge is almost as high as the bimodal one when $R_2^0 = 3.0 \times 10^{-3}$ cm (not illustrated), whereas $T_{Gi}$ near the inner cluster edge (innermost radial coordinate where all size classes coexist) is lower than for either bimodal calculations because of the higher $n$. With the exception of this particular location, the initial-size-class-1 drops evaporate at the same rate as in the bimodal distributions having $R_2^0 = 3.0 \times 10^{-3}$ cm, but the value of $n_1^0$ is slightly lower. The introduction of the third initial drop size lowers $n_2^0$ by about 20%, a significant impact causing smaller centrifugation of this additional class and slightly slower evaporation rate towards the outer cluster edge. The lower evaporation rate also observed towards the inner cluster edge is, as explained above, attributed to the lower $T_{Gi}$ at that location. The evaporation rate of the third class is considerably lower near both inner and outer boundaries than for the bimodal distribution, despite having less than half the initial drop number density. The larger drop sizes enhance centrifugation of this third class, particularly at the inner cluster boundary.

To summarize the above discussion, polydispersity both enhances penetration of the evaporated compound into the surroundings and increases the maximum $Y_F$ within the cluster. Thus, polydispersity is recommended to enhance spray combustion.

Since polydispersity benefits spray combustion, it is important to find how the relative number of drops in the initial size distribution impacts the quantity and distribution of the evaporated compound. Calculations were therefore performed with $\max_{r_j^0}(n_j^0)$ switched between the two initial size classes for a situation that was otherwise baseline. This switch decreased $n$ (by about 25%) since more mass is contained in the initially larger-size class drops which now have a much larger drop number density. Comparisons with the baseline case show that centrifugal effects depend on $n$ and for the same mass, a smaller $n$ results in smaller centrifugation. Comparisons between early time behavior show that evaporation is now slower and the evaporated compound penetrates the surroundings less. Thus, it is recommended for spray combustion that a polydisperse distribution should contain a proportionally larger number of small drops.

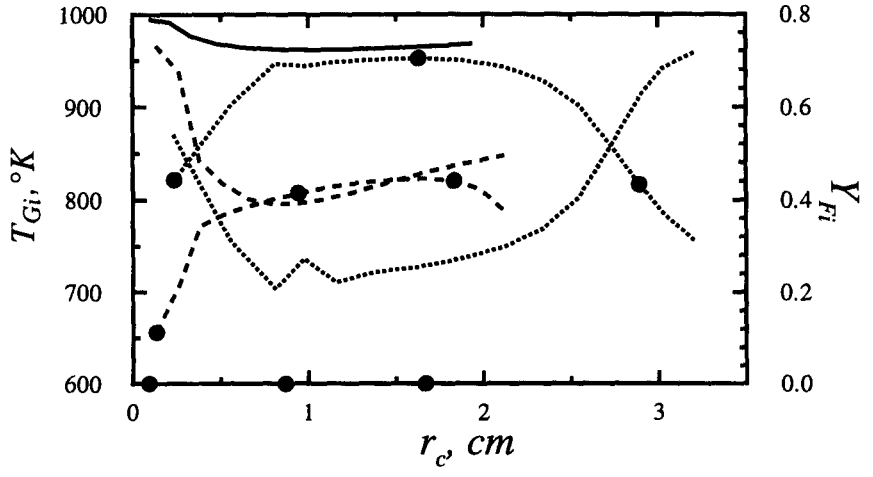


Figure 16. Interstitial gas temperature and mass fraction of the evaporated compound vs the radial coordinate for a trimodal distribution with $R_1^0 = 2.0 \times 10^{-3}$ cm, $R_2^0 = 2.5 \times 10^{-3}$ cm, and $R_3^0 = 3.0 \times 10^{-3}$ cm. All other initial conditions and parameters are listed in the figure 2 caption.

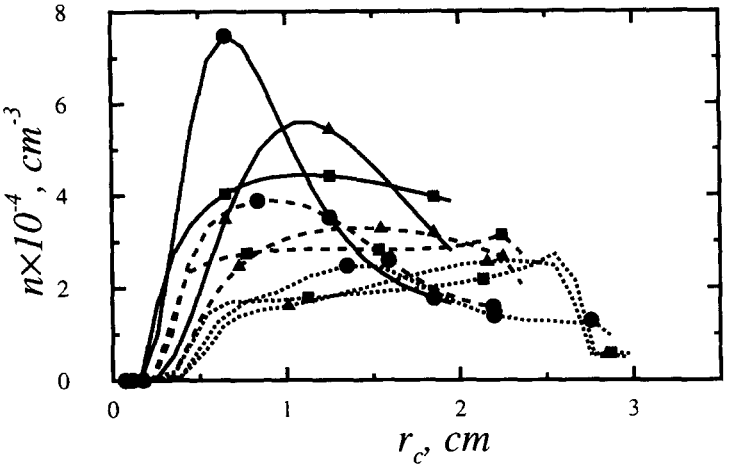


Figure 17. Comparison of the drop number densities vs radial coordinate for: $q_1 = q_2 = 0.5$, $\alpha_1 = \alpha_2 = 0.5$ (■); $q_1 = q_2 = 2.5$, $\alpha_1 = \alpha_2 = 0.5$ (▲); $q_1 = 2.5$, $q_2 = 0.5$, $\alpha_1 = 0.25$, $\alpha_2 = 0.5$ (●) at $7 \times 10^{-5}$ s (solid lines), $2.2 \times 10^{-3}$ s (dashed lines) and $8.4 \times 10^{-3}$ s (dotted lines). All other initial conditions and parameters are listed in the figure 2 caption.

### 5.4. *Effect of the initial drop number distribution, $n^0$, profile*

Given the uncertainties in measurements of $n^0$ (Presser *et al.* 1994), $q_j$ and $\alpha_j$ (see [30] and [33]) have been varied to change the width and the location of the peak of the distribution $n^0(r^0)$. In one calculation $q_1 = 2.5$ and $\alpha_1 = 0.25$ while $q_2$ and $\alpha_2$ retain their baseline values of 0.5 and 0.5 respectively; in another calculation $q_1 = q_2 = 2.5$ and $\alpha_1 = \alpha_2 = 0.5$. Additionally, a calculation (discussed above) with a monodisperse drop collection has also been performed with $q = 10^{-3}$ and $R^0 = 2 \times 10^{-3}$ cm to simulate a uniformly-distributed, monodisperse cluster (e.g. Bellan and Harstad 1990). In all these calculations $\Phi^0 = 0.314$ and the other initial conditions are those of the baseline calculation (see figure 2 caption). The evolution of $n$ for all the different bimodal distributions is illustrated in figures 14 and 17.

An initially monodisperse, uniformly-distributed collection of drops quickly develop nonuniformities in $T_{Gi}$ and $R_j$, thereby invalidating the monodisperse assumption in time-dependent calculations for initially dense sprays. However, figure 14 shows that $n$ remains uniform in the central cluster, although nonuniformities develop towards the inner and outer boundaries. Thus, if boundary effects are unimportant, the uniform $n$ assumption might have some validity for engineering calculations. These results are consistent with those found for a binary size distribution in section 5.3.

The effect of larger $n^0$ gradients was investigated using $q_1 = q_2 = 2.5$ (the baseline value is 0.5). Figure 17 shows that in this case extremely dense regions of drops exist at the cluster center where the drops are just a few diameters apart. Examination of the drop size distribution shows that in the central cluster the residual drops are larger, and thus take longer to evaporate.

Despite the more nonuniform initial drop size distribution, time relaxation still causes the majority of the cluster (excluding about 15–20% where edge effects are important) to have a distribution that increases with radial location; however, the gradients are now larger.

The effect of different initial maxima and different skewness for the two initial size classes has been investigated by setting $\alpha_1 = 0.25$, $\alpha_2 = 0.5$, $q_1 = 2.5$ and $q_2 = 0.5$, rendering $n_1^0$ narrower and peaked closer to the inner cluster boundary. The different locations of the $n_1^0$ and $n_2^0$ maxima produce a nonmonotonic $n^0$ peaked at the same radial position as the more numerous initial-size-class-1 drops. Examination of the results shows that the minimum in $T_{Gi}$ corresponds to a maximum in $n_2$. The low $T_{Gi}$ in the cluster center affects drop evaporation; pockets of relatively large drops are long-lived for both initial-size classes, and at the end of the calculation an unevaporated pocket of initial-size-class-2 drops remains in the minimum $T_{Gi}$ region. Eventually, the initial-size-class-2 drops are concentrated near the inner and outer cluster peripheries, whereas most initial-size-class-1 drops are in the central cluster.

The different $n_j^0$ profiles presented here illustrate only a few possible configurations, but demonstrate that the behavior of a cluster of drops is highly sensitive to the initial conditions. Thus, when comparing numerical results to experimental observations, it is essential that the same initial conditions be used.

### 5.5. *Effect of transport from the surrounding to the cluster*

Section 2 showed that heat and mass transfer from the cluster to the surroundings are modeled globally using $Nu_c$. The constant $C_1$ appearing in $Nu_c$ was assumed to be 0.35 in all above calculations. To see the effect of $C_1$ calculations are performed with $C_1 = 0.175$, a value which reduces heat and mass transfer to the cluster lowering the outer $T_{Gi}$; results are not illustrated for the sake of brevity. At the outer cluster edge, $T_{Gi}$ is now 10% lower than for typical previous cases, causing a reduction in the evaporation rate, and so giving slightly larger drops near the outer cluster boundary. Although the outer evaporation rate is now lower, $Y_F$ is larger by about 20% at the cluster outer edge because less air enters the cluster from the surroundings. Because $Y_F$ is now larger, the evaporated species flux and the gas flux towards the vortex core also increase. These changes affect only the outer third of the cluster. Thus, when $\Phi^0 = 0.314$, a 50% reduction in $C_1$ results in a maximum reduction of 10% in $T_{Gi}$ and a maximum increase of 20% in $Y_F$ in the outer third of the cluster. This effect is expected to become less important as $\Phi^0$ increases.

### 5.6. *Effect of small scale turbulence*

As discussed in section 2, small scale turbulence is modeled using a global turbulent viscosity proportional to the constant $C_T$. Varying $C_T$ shows how azimuthal drop motion affects small scale turbulent features.

Calculations were performed for $\Phi^0 = 0.314$ with $C_T = 10^{-2}$ to simulate a five-fold turbulence reduction in the interior of the cluster and $C_1 = 7 \times 10^{-2}$ to simulate an identical reduction at its boundaries; results are not illustrated due to space constraints. The most obvious effects of turbulence reduction were a 14% decrease in $T_{Gi}$ towards the outer cluster and at the outer edge, the formation of a peak in both $n_j$s at the inner cluster boundary, a reduction in $n_j$s at the outer cluster boundary, a more uniform profile of $n$ (including a reduction in the gradients at the outer cluster boundary), and increased drop centrifugation.

The $T_{Gi}$ reduction is caused by the decreased heat transfer from the surroundings to the cluster through the reduction of $C_1$. This in turn lowers drop temperature and increases $R_j/R_j^0$ at the outer cluster edge which together with a larger $u_{dr_j}$ increases drop centrifugation. This interpretation is corroborated by the larger angle of $\mathbf{u}_d$ with the tangent at a fixed radial location.

The formation of a peak in $n_j$ is associated with the consecutive coordinate annuli becoming thinner for smaller $C_T$. Plots of radial locations versus time show that in the baseline calculation the distance between consecutive radial locations increases with time or remains constant everywhere; now this still occurs except at the inner cluster edge where this distance becomes smaller with time. This indicates that small scale turbulence disperses drops at the microscale.

## 6. SUMMARY AND CONCLUSIONS

The statistical model presented here describes the dynamics and evaporation of a polydisperse cluster of liquid drops in a gaseous, cylindrical, axisymmetric, infinite inviscid vortex. This model includes two-way coupling between gas and drops, both dynamically and thermodynamically, and accounts for multiparticle interactions in terms of motion, heating and evaporation. Thus, this model can describe both dense and dilute drop clusters. 'Denseness' is defined in terms of the ratio of the average distance between the centers of adjacent drops to the average drop diameter.

The initial drop size distribution is partitioned into initial-size classes which develop their own, continuous, drop size distribution in a coordinate system moving with the initial-size class.

The major results of this study, obtained by varying critical parameters in numerical calculations, are:

(1) The drops at the cluster periphery act as a screen for heat transfer from the cluster surroundings, thus causing nonuniformities within the cluster.

(2) Size-differentiated centrifuging, which occurs for drops in cold flows, does not necessarily occur in vortices where the initial gas temperature is larger than that of the drops.

(3) Polydispersity increases the maximum of the evaporated compound mass fraction within the cluster and penetration of the evaporated compound into the surroundings. It is recommended for spray combustion to have a proportionally larger fraction of small drops to enhance evaporation; the required minority of larger drops provide centrifugation-induced penetration of the vapor into the ambient.

The model has been qualitatively validated with spray observations. Uncertainties due to the modeling of heat transfer between cluster and surrounding gas through a Nusselt number, and to the nature of the modeling of small scale turbulence coupling to drop motion (which has been incorporated descriptively, but not derived from first principles) have been addressed through parametric variations of the only two free parameters of the model. Future investigations will provide a more detailed consideration of turbulence and also of the outer boundary and adjacent surrounding regions of the cluster.

*Acknowledgements*—This research was conducted at the Jet Propulsion Laboratory and sponsored by the U.S. Air Force Wright Laboratory, Aero Propulsion and Power Directorate, with Dr T. Jackson serving as contract monitor, under an agreement with the National Aeronautics and Space Administration.

## REFERENCES

Abramzon, B. and Sirignano, W. A. (1989) Droplet vaporization model for spray combustion. *Int. J. Heat Mass Transfer* **32,** 1605–1618.

Aftel, R., Gupta, A. K., Cook, C. and Presser, C. (1996) Gas property effects on droplet atomization and combustion in an 'air-assist' atomizer. *Proceedings of the 26th Symp. (Int.) on Combustion*, Naples, Italy.

Akamatsu, F., Mizutani, Y., Kasuki, M., Tsushima, S. and Cho Y. D. (1996) Measurement of local group combustion number of droplet clusters in a premixed spray system. *Proceedings of the 26th Symp. (Int.) on Combustion*, Naples, Italy.

Allen, M. G. and Hanson, R. K. (1986) Digital imaging of species concentration fields in spray flames. *21st Symp. (Int.) on Combustion*, pp. 1755–1762.

Allen, M. G. and Hanson, R. K. (1986) Planar laser-induced-fluorescence monitoring of OH in a spray flame. *Optica Engineering* **25,** 1309–1311.

Bellan, J. and Cuffel, R. (1983) A theory of non dilute spray evaporation based upon multiple drop interactions. *Combust. and Flame* **51,** 55–67.

Bellan, J. and Harstad, K. (1987) The details of the convective evaporation of dense and dilute clusters of drops. *Int. J. Heat Mass Transfer* **30,** 1003–1093.

Bellan, J. and Harstad, K. (1988) Turbulence effects during the evaporation of drops in clusters. *Int. J. Heat Mass Transfer* **31,** 1655–1668.

Bellan, J. and Harstad, K. (1990) The dynamics of dense and dilute clusters of drops evaporating in large, coherent vortices. *23rd Symp. (Int.) on Combustion*, pp. 1375–1381.

Chung, J. N. and Troutt, T. R. (1988) Simulation of particle dispersion in an axisymmetric jet. *J. Fluid Mech.* **186,** 199–222.

Cliffe, K. A. and Lever, D. A. (1985) Isothermal flow past a blowing sphere. *Int. J. Numer. Meth. Fluids* **5,** 709–725.

Crowe, C. T., Chung, J. N. and Troutt, J. R.(1988) Particle mixing in free shear flows. *Prog. Energy Combust. Sci.* **14,** 171–194.

Crowe, C. T., Chung, J. N. and Troutt, J. R. (1993) Particle dispersion by organized turbulent structures. In *Particulate Two Phase Flow*, ed. M. Roco, Ch. 18. Butterworth, London.

Crowe, C. T., Troutt, J. R. and Chung, J. N. (1996) Numerical models for two-phase turbulent flows. *Annu. Rev. Fluid Mech.* **28,** 11–43.

Engelbert, C., Hardalupas, Y. and Whitelaw, J. H. (1995) Breakup phenomena in coaxial airblast atomizers. *Proc. R. Soc. Lond.* **451,** 189–229.

Gupta, A. K., Presser, C., Hodges, J. T. and Avedesian, C. T. (1996) Role of combustion on droplet transport in pressure-atomized spray flames. *Journal of Propusion and Power* **12,** 543–553.

Hardalupas, Y., Liu, C. H. and Whitelaw, J. H. (1994) Experiments with disk stabilized kerosene-fuelled flames. *Comb. Sci. and Tech.* **97,** 157–191.

Harstad, K. and Bellan, J. (1991) A model of the evaporation of binary-fuel clusters of drops. *Atomization and Sprays* **1,** 367–388.

Hidy, G. M. and Brock, J. R. (1970) *The Dynamics of Aerocoloidal Systems*, International Reviews in Aerosol Physics and Chemistry, Vol. 1. Pergamon Press, Oxford.

Lazaro, B. J. and Lasheras, J. C. (1989) Particle dispersion in a turbulent, plane, free shear layer. *Phys. Fluids A* **1,** 1035–1044.

Lazaro, B. J. and Lasheras, J. C. (1992a) Particle dispersion in the developing free shear layer. Part 1. Unforced flow. *J. Fluid Mech.* **235,** 143–178.

Lazaro, B. J. and Lasheras, J. C. (1992b) Particle dispersion in the developing free shear layer. Part 2. Forced flow. *J. Fluid Mech.* **235,** 197–221.

Longmire, E. K. and Eaton, J. K. (1992) Structure of a particle-laden round jet. *J. Fluid Mech.* **236,** 217–257.

Maxey, M. R. and Riley, J. J. (1983) Equation of motion for a small rigid sphere in a nonuniform flow. *Phys. Fluids* **26,** 883–889.

McDonell, V. G., Adachi, M. and Samuelsen, G. S. (1992) Structure of reacting and non-reacting swirling air-assisted sprays. *Comb. Sci. and Tech.* **82,** 225–248.

McDonell, V. G., Adachi, M. and Samuelsen, G. S. (1993) Structure of reacting and non-reacting non-swirling air-assisted sprays, Part II: Drop behavior. *Atomization and Sprays* **4,** 411–436.

Mizutani, Y., Nakabe, K., Fuchihata, M., Akamatsu, F., Zaizen, M. and El-Emam, S. H. (1993) Spark-ignited spherical flames propagating in a suspended droplet cloud. *Atomization and Sprays* **3,** 125–135.

Nakabe, K., Mizutani, Y., Akamatsu, F. and Fujoka, H. (1994) Observation of droplet group combustion in terms of simultaneous measurement of Mie scattering and spray flames. *Atomization and Sprays* **4,** 485–500.

Nieh, S. and Zhang, J. (1992) Simulation of the strongly swirling aerodynamic field in a vortex combustor. *J. of Fluid Engineering* **114,** 367–374.

Presser, C., Santoro, R. J. and Semerjian, H. G. (1986) Velocity and droplet size measurements in a fuel spray. AIAA-86-0297, presented at the 24th Aerospace Sciences Meeting, Reno, NV.

Presser, C. and Semerjian, H. G. (1988) Dynamics of pressure-jet and air-assisted nozzle sprays: aerodynamic effects. AIAA-88-3139, presented at the AIAA/ASME/SAE/ASEE 24th Joint Propulsion Conference, Boston, MA.

Presser, C., Gupta, A. K., Avedesian, C. T. and Semerjian, H. G. (1992) Combustion of methanol and methanol/dodecanol spray flames. *Journal of Propulsion and Power* **8,** 553–559.

Presser, C., Gupta, A. K. and Semerjian, H. G. (1993) Aerodynamic characteristics of swirling spray flames: pressure-jet atomizer. *Combust. Flame* **92,** 25–44.

Presser, C., Gupta, A. K., Avedesian, C. T. and Semerjian, H. G. (1994) Effect of dodecanol content on the combustion of methanol spray flames. *Atomization and Sprays* **4,** 207–222.

Raju, M. S. and Sirignano, W. A. (1987) Spray computations in a centerbody combustor. *Proc. of the* 1987 *ASME/ISME Thermal Eng. Joint Conf., ASME*, Vol. 1, pp. 61–71.

Rudoff, R. C., Brena de le Rosa, A., Sankar, S. V. and Bachalo, W. D. (1989) Time analysis of polydisperse sprays in complex turbulent environments. AIAA-89-0052, presented at the 27th Aerospace Sciences Meeting, Reno, NV.

Schubauer, G. B. and Tchen, C. M. (1959) Turbulent flow. *Turbulent Flows and Heat Transfer, High Speed Aerodynamics and Jet Propulsion*, pp. 75–195, ed. C. C. Liu. Princeton University Press, New York.

Seth, B., Aggarwal, S. K. and Sirignano, W. A. (1980) Flame propagation through an air-fuel spray mixture with transient droplet vaporization. *Combustion and Flame* **39,** 149–168.

Squires, K. D. and Eaton, J. K. (1991) Preferential concentration of particles by turbulence. *Phys. Fluids A* **3,** 1169–1178.

Tambour, Y. (1985) A Lagrangian sectional approach for simulating droplet size distribution of vaporizing fuel sprays a turbulent jet. *Combustion and Flame* **60,** 15–28.

Tambour, Y. (1994) Effects of multisize droplet distributions on polydisperse spray jet far-field diffusion flames. *Atomization and Sprays* **4**, 565–582.
Williams, F. (1965) *Combustion Theory*. Addison-Wesley, Boston.
Yang, M. and Sichel, M. (1989) Interaction of droplet clouds with swirling flows. AIAA-89-0159, presented at the 27th Aerospace Sciences Meeting, Reno, NV.

## APPENDIX A

*Singularity Analysis of Solutions of the Drops Conservation Equations*

For simplicity, the case of a single drop size class without turbulent diffusion or $\hat{p}$ is examined here. The goal is to determine whether the system of equations possesses a nonsingular (regular) solution for any initial conditions, and if not to identify a set of initial conditions for which the solution is regular, at least for short times. Following the equations given in section 2.1, the drops equations are

$$\mathrm{d}r/\mathrm{d}t = u_{\mathrm{dr}} \tag{A1}$$

$$\mathrm{d}u_{\mathrm{dr}}/\mathrm{d}t = u_{\mathrm{d}\theta}^2/r - v_{\mathrm{s}}(u_{\mathrm{dr}} - u_{\mathrm{Gr}}) \tag{A2}$$

$$\mathrm{d}\Gamma_{\mathrm{d}}/\mathrm{d}t = -v_{\mathrm{s}}(\Gamma_{\mathrm{d}} - \Gamma_{\mathrm{G}}), \tag{A3}$$

where $\Gamma_{\mathrm{d}} \equiv ru_{\mathrm{d}\theta}$, $\Gamma_{\mathrm{G}} \equiv ru_{\mathrm{G}\theta}$ and

$$\partial n/\partial t + [\partial(ru_{\mathrm{dr}}n)/\partial r]/r = 0. \tag{A4}$$

The Lagrangian radial coordinates associated with the drop are $r = r(t, r^0)$, where $r^0$ is the position at $t = 0$, and the initial condition for the radial velocity is $u_{\mathrm{dr}}(0, r^0)$.

If a solution of this system of equations exists at $t > 0$, then that means that there exists a one-to-one transformation between $r$ and $r^0$ and the mapping $r^0 \to r$ is nonsingular. The Jacobian of this mapping is

$$J \equiv \partial r/\partial r^0 = J(t, r^0) \tag{A5}$$

with $J(0, r^0) = 1$.

For specified $u_{\mathrm{G}\theta}(t, r) = u_{\mathrm{G}\theta}(t, r^0)$, [A3] can be solved to yield

$$\Gamma_{\mathrm{d}} = \Gamma_{\mathrm{d}}^0 \exp\left(-\int_0^t v_{\mathrm{s}}\,\mathrm{d}t'\right) + \int_0^t v_{\mathrm{s}}\Gamma_{\mathrm{G}} \exp\left(-\int_{t'}^t v_{\mathrm{s}}\,\mathrm{d}t''\right)\mathrm{d}t'. \tag{A6}$$

Since for low Reynolds numbers $v_{\mathrm{s}} = D_{\mathrm{s}}/R^2$, where $D_{\mathrm{s}} = 9\,\mu_{\mathrm{G}}/(2\rho_{\mathrm{L}}) \simeq 10^{-4}\,\mathrm{cm}^2/\mathrm{s}$ and $R = O(10^{-3})\,\mathrm{cm}$, then $v_{\mathrm{s}} \gg 1$. Equation [A6] shows that if $\int_0^t v_{\mathrm{s}}\mathrm{d}t' \ll 1$, then $\Gamma_{\mathrm{d}} \simeq \Gamma_{\mathrm{d}}^0 = r^0 u_{\mathrm{d}\theta}^0(r^0)$ and if $\int_0^t v_{\mathrm{s}}\,\mathrm{d}t' \gg 1$, then $\Gamma_{\mathrm{d}} \simeq \Gamma_{\mathrm{G}}$, $u_{\mathrm{d}\theta} \simeq u_{\mathrm{G}\theta}$.

The momentum equations can be expressed in terms of $J$ for a drop annulus, $\Delta r^0$, initially located at $r^0$, at $t > 0$

$$\Delta r = J\Delta r^0 \tag{A7}$$

$$\Delta(\mathrm{d}r/\mathrm{d}t) = \Delta u_{\mathrm{dr}} = (\Delta r^0)\mathrm{d}J/\mathrm{d}t \tag{A8}$$

$$\Delta(\mathrm{d}u_{\mathrm{dr}}/\mathrm{d}t) = (\Delta r^0)(\mathrm{d}^2J/\mathrm{d}t^2) \tag{A9}$$

$$\Delta u_{\mathrm{d}\theta} = (\Delta r^0)(\partial u_{\mathrm{d}\theta}/\partial r)J \tag{A10}$$

$$\Delta u_{\mathrm{Gr}} = (\Delta r^0)(\partial u_{\mathrm{Gr}}/\partial r)J, \tag{A11}$$

where $\Delta$ represents the difference between the values of the variables at the two extreme positions defining an annulus. This means that from [A2]

$$\Delta(\mathrm{d}u_{\mathrm{dr}}/\mathrm{d}t) = (2u_{\mathrm{d}\theta}/r)\Delta u_{\mathrm{d}\theta} - (u_{\mathrm{d}\theta}/r)^2(\Delta r) - v_{\mathrm{s}}(\Delta u_{\mathrm{dr}} - \Delta u_{\mathrm{Gr}}). \tag{A12}$$

The above equation can be interpreted as a differential equation for $J$

$$d^2J/dt^2 + v_s\, dJ/dt + (\omega^2 - 2\omega\, \partial u_{d\theta}/\partial r - v_s\, \partial u_{Gr}/\partial r)J = 0, \qquad [A13]$$

where $\omega = d\theta/dt = u_{d\theta}/r$, $\theta$ is the azimuthal angle change, and for short times $\omega = r^0 u^0_{d\theta}/r^2$.

Equation [A4] gives

$$\frac{d}{dt}\int_{\Delta r} nr\, dr = 0 \qquad [A14]$$

$$nr\Delta r = n^0 r^0 \Delta r^0 \qquad [A15]$$

or $nrJ = n^0 r^0$. Also,

$$r = \int_0^{r^0} J(t, r^0) dr^0. \qquad [A16]$$

Through the gas energy equation $u_{Gr}$ depends upon $n$ and since $n$ depends upon $J$, $u_{Gr}$ depends upon $J$. The coefficient of $J$ in [A13] depends upon $J$, making it very difficult to obtain a solution. However, since $J$ has an oscillatory form with a damping component, $J$ becoming null during the drops lifetime depends upon the relative magnitude of the damping component with respect to the frequency of the oscillation. A sufficient condition for $J$ to be non null is that [A13] be quasi-steady; thus $J$ is a strictly positive constant and

$$\omega^2 - 2\omega\, \partial u_{d\theta}/\partial r - v_s\, \partial u_{Gr}/\partial r = 0. \qquad [A17]$$

If $u^0_{dr} = 0$, then $(dJ/dt)^0 = 0$. $(d^2J/dt^2)^0 = 0$ if $(du_{dr}/dt)^0 = A^0$, where $A^0$ is a constant. Using the momentum equation one obtains

$$(u^0_{d\theta})^2/r^0 = A^0 - v^0_s u^0_{Gr}. \qquad [A18]$$

In order to satisfy the above relationship for all $r$, $A^0 \geqslant v^0_s \max(u^0_{Gr})$ is chosen.